Supporting Information for:

Hybrid bronzes: mixed-valence organic-inorganic metal oxides as a tunable material platform

W. Lakna N. Dayaratne,[‡a] Raúl Torres-Cadena,[‡a] Bennett P. Schmitt,[a] Emma M. Westrick,[a] and Adam Jaffe[*a]

[a]*Department of Chemistry and Biochemistry, University of Notre Dame, Notre Dame, Indiana 46556, USA*
[‡] *These authors contributed equally*

*ajaffe@nd.edu

Experimental details

Figures S1–S38

Tables S1–S5

References

Experimental details

Solvents were of reagent grade or higher purity. All reagents were purchased from commercial vendors and used as received. All experiments were conducted in air unless stated otherwise. Abbreviations used: 4,4'-bipy = 4,4'-bipyridine, pyz = pyrazine, azp = 4,4'-azopyridine, 4,4'-bipy-ethane = 4,4'-ethylenedipyridine, 4,4'-bipy-ethene = 4,4'-vinylenedipyridine, dps = 4,4'-dipyridyl disulfide, 4*H*-trz = 4*H*-1,2,4-triazole, py = pyridine, py-4-vinyl = 4-vinyl pyridine, py-4-OH = 4-hydroxypyridine.

Synthesis of $H_{0.33}MoO_3$

MoO_3 (0.33 g, 2.3 mmol) was placed in a round bottom flask with 15 mL of 4 M HCl, followed by the addition and dissolution of $SnCl_2$ (0.75 g, 3.9 mmol) which resulted in an immediate color change from white to grey followed by a gradual change to blue. This molybdenum oxide suspension was stirred for 15 minutes at room temperature. The resulting blue crystalline powder was then isolated via centrifugation followed by thorough washing with deionized water (3 × 15 mL) until the pH of the water was approximately 4. The powder was then washed with acetone (1 × 15 mL) and allowed to dry in air. We note that structurally distinct type I H_xMoO_3 is reported for $0.23 < x < 0.4$,[1] therefore small variation in level of reduction is expected.

Synthesis of $H_{1.68}MoO_3$

A round bottom flask was charged with MoO_3 (1.00 g, 6.95 mmol), 50 mL of 12 M HCl, and a magnetic stir bar. To this stirring suspension, 0.32 g (4.9 mmol) of Zn powder was gradually added during which vigorous bubbling was observed. After completing the Zn addition, the reaction mixture was allowed to stir at room temperature for 2 hours. Afterward, the burgundy crystalline solid was isolated via centrifugation and washed with deionized water until the pH of the water was approximately 4. The solid was then washed with acetone (1 × 15 mL) and allowed to dry in air. We note that structurally distinct type III H_xMoO_3 is reported for $1.55 < x < 1.72$,[1] therefore small variation in level of reduction is expected.

Synthesis of $H_{0.95}MoO_3$

$H_{1.68}MoO_3$ (1.0 g) was heated in a round bottom flask at 95 °C for 1.5 hours in air, yielding a dark blue microcrystalline product. We note that structurally distinct type II H_xMoO_3 is reported for $0.85 < x < 1.04$,[1] therefore small variation in level of reduction is expected.

Synthesis of pyridine-, pyrazine-, and piperazine-intercalated products

The intercalated products were synthesized via a slight modification of a prior literature report.[2] A 20 mL vial was charged with $H_{0.33}MoO_3$ (0.10 g, 0.69 mmol), the ligand in excess, 4 mL of toluene, and a magnetic stir bar. The resulting suspension was stirred at 80 °C for a period of time according to Table S1:

Ligand	Reaction Temperature (°C)	Reaction Duration
pyridine	80	24 h
pyrazine	100	5 d
piperazine	80	6 h

Table S1. Intercalation conditions for aliphatic and aromatic amines in H_xMoO_3

The resulting crystalline intercalated solids were washed with acetone (2 × 10 mL) and allowed to dry in air. In an alternative method, the intercalated products were also synthesized using the above quantities and procedures but at room temperature.

Synthesis of $(4,4'\text{-bipy})_{0.5}MoO_3$ (4,4'-bipy = 4,4'-bipyridine)

Single crystals and microcrystalline powders of $(4,4'\text{-bipy})_{0.5}MoO_3$ were synthesized according to previous literature reports.[3-4]

**Unless otherwise noted, all hybrid organic-inorganic metal oxides and hybrid bronzes described below were washed in the same manner: after cooling the reaction to room temperature, the product was isolated via centrifugation followed by water washes (2 × 10 mL) and washes with isopropanol (2 × 10 mL).*

Synthesis of $(4,4'\text{-bipy})_{0.5}H_xMoO_3$

Multiple synthesis methods were used to obtain $(4,4'\text{-bipy})_{0.5}H_xMoO_3$. In the first method, a 23 mL PTFE-lined pressure vessel was charged with $H_{0.33}MoO_3$ (0.05 g, 0.3 mmol), 4,4'-bipy (0.050 g, 0.32 mmol), and 10 mL of deionized water. The PTFE-lined vessel was heated at 150 °C for 3 days, yielding black microcrystalline powder. Reduction was also performed according to a newly developed and more facile stirring method, as mentioned in the main text, that yielded microcrystalline powders. Here, a 20 mL vial was charged with $H_{0.33}MoO_3$ (0.10 g, 0.69 mmol), 4,4'-bipy (0.10 g, 0.66 mmol), and 10 mL of deionized water. The resulting suspension was allowed to stir at 80 °C for 3 days. Alternatively, a 20 mL vial was charged with MoO_3 (0.127 g, 0.882 mmol), 4,4'-bipy (69 mg, 0.44 mmol), Mo metal (either 3 mg [0.03 mmol], 5 mg [0.05 mmol], 10 mg [0.1 mmol], 10 mg [0.1 mmol] under inert conditions, or 15 mg [0.15 mmol] to vary the reduction level), and 10 mL of deionized water. The resulting suspension was allowed to stir at 80 °C for 5 days, resulting in a dark green microcrystalline product.

Synthesis of $(4,4'\text{-bipy})_{0.5}WO_3$

Microcrystalline powders of $(4,4'\text{-bipy})_{0.5}WO_3$ were synthesized according to previous literature reports.[3,5] This material can also be synthesized through our newly developed facile stirring method in which a 20 mL vial was charged with $3Na_2WO_4{\cdot}9WO_3{\cdot}H_2O$ (0.1 g, 0.03 mmol), an excess of 4,4'-bipy (0.094 g, 0.60 mmol), and 10 mL of deionized water. The reaction was heated to 80 °C with constant stirring for 3 days, yielding yellow microcrystalline powder. This reaction can also be carried out by substituting $3Na_2WO_4{\cdot}9WO_3{\cdot}H_2O$ with $WO_3{\cdot}H_2O$.

Synthesis of $(4,4'\text{-bipy})_{0.5}H_xWO_3$

A 23 mL PTFE-lined pressure vessel was charged with $3Na_2WO_4{\cdot}9WO_3{\cdot}H_2O$ (0.1 g, 0.03 mmol), 4,4'-bipy (0.0627 g, 0.400 mmol), W metal (0.017 g, 0.10 mmol), and 10 mL of deionized water. The PTFE-lined vessel was heated to 170 °C for 2 days, yielding dark blue single crystals suitable for X-ray structure determination and microcrystalline powder. The same procedure run for 7 days and with all reagents increased in concentration by threefold yielded microcrystalline powder featuring a higher reduction level. Alternatively, a 20 mL vial was charged with $(4,4'\text{-bipy})_{0.5}WO_3$ (25 mg, 0.081 mmol) and 5 mL of a 0.5 M aqueous solution of $Na_2S_2O_4$. The reaction mixture was allowed to stir under room temperature for 24 hours. A dark green microcrystalline powder was isolated.

Synthesis of $(pyz)_{0.5}H_xMoO_3$ (pyz = pyrazine)

A 23 mL PTFE-lined pressure vessel with $(NH_4)_6Mo_7O_{24}$ (64 mg, 0.055 mmol), pyz (18 mg, 0.23 mmol), Mo (5 mg, 0.05 mmol) in 10 mL of H_2O. The PTFE-lined vessel was heated to 170 °C for 7 days, yielding black, block-shaped single crystals suitable for X-ray structure determination and microcrystalline powder. This material also can be synthesized using our stirring method in which a 20 mL vial is charged with MoO_3 (64 mg, 0.44 mmol), pyz (18 mg, 0.23 mmol), Mo metal (either 3 mg [0.03 mmol], 5 mg [0.05 mmol], or 10 mg [0.1 mmol] to vary the reduction level), and 10 mL of deionized water, followed by heating to 80 °C with constant stirring for 7 days, yielding black microcrystalline powder.

Synthesis of $(pyz)_{0.5}WO_3$

Single crystals and microcrystalline powders of $(pyz)_{0.5}WO_3$ were synthesized in a modification of previous literature reports.[3,5] A 23 mL PTFE-lined pressure vessel was loaded with $3Na_2WO_4{\cdot}9WO_3$ (0.10 g, 0.033 mmol), an excess of pyz (0.048 g, 0.60 mmol), and 6 mL of deionized water. The PTFE-lined vessel was heated to 160 °C for 7 days, yielding orange single crystals and microcrystalline powder. Alternatively, in our stirring method, a 20 mL vial was charged with $WO_3{\cdot}H_2O$ (0.10 g, 0.35 mmol), pyz (0.048 g, 0.60 mmol), and 10 mL of deionized water. The reaction was heated to 80 °C with constant stirring for 3 days, yielding yellow microcrystalline powder.

Synthesis of $(pyz)_{0.5}H_xWO_3$

A 23 mL PTFE-lined Pressure vessel with $3Na_2WO_4{\cdot}9WO_3{\cdot}H_2O$ (0.3 g, 0.1 mmol), pyz (1.21 mmol), W (0.030 g, 0.163 mmol), and 10 mL of deionized water. The PTFE-lined vessel was heated to 170 °C for 7 days, yielding black microcrystalline powder.

Synthesis of $(azp)_{0.5}MoO_3$ (azp = 4,4'-azopyridine)

According to our mild stirring method, a 20 mL vial was charged with $(NH_4)_6Mo_7O_{24}$ (0.116 g, 0.0996 mmol), azp (64 mg, 0.35 mmol), and 10 mL of deionized water. The reaction was heated to 80 °C with constant stirring for 3 days, yielding orange microcrystalline powder. To synthesize single crystals, a 20 mL vial was charged with $(NH_4)_6Mo_7O_{24}$ (0.027 g, 0.023 mmol), azp (8 mg, 0.04 mmol), and 7 mL of deionized water and placed in an oven. The temperature was raised to 95 °C and maintained for 24 hours, then lowered to 80 °C and maintained for another 72 hours. The temperature was then lowered to room temperature, after which orange plate-shaped single crystals suitable for X-ray structure determination were collected.

Synthesis of $(azp)_{0.5}H_xMoO_3$

A 20 mL vial was charged with MoO_3 (50 mg, 0.35 mmol), azp (32 mg, 0.17 mmol), $Na_2S_2O_4$ (87 mg, 0.5 mmol), and 10 mL of deionized water, followed by heating to 80 °C with constant stirring for 5 days, yielding black microcrystalline powder.

Synthesis of $(azp)_{0.5}WO_3$

A 23 mL PTFE-lined pressure vessel was charged with $3Na_2WO_4{\cdot}9WO_3{\cdot}H_2O$ (0.10 g, 0.033 mmol), azp (55.5 mg, 0.301 mmol), and 6 mL of deionized water. The reaction was heated to 150 °C for 4 days, yielding orange plate-shaped single crystals and microcrystalline powder. However, the single crystals were not of sufficient size for structure determination via single-crystal X-ray diffraction measurements. When synthesized according to our stirring reaction, a 20 mL vial was charged with $3Na_2WO_4{\cdot}9WO_3{\cdot}H_2O$ (0.10

g, 0.033 mmol), azp (55.5 g, 0.301 mmol), and 10 mL of deionized water. The reaction was heated to 80 °C with constant stirring for 3 days, yielding orange microcrystalline powder. This reaction can also be carried out by substituting $3Na_2WO_4{\cdot}9WO_3{\cdot}H_2O$ with $WO_3{\cdot}H_2O$.

Synthesis of (4,4'-bipy-ethane)$_{0.5}$WO$_3$[3] (4,4'-bipy-ethane = 4,4′-ethylenedipyridine or 1,2-di(4-pyridyl)ethane)

Under mild stirring conditions, a 20 mL vial was charged with $WO_3{\cdot}H_2O$ (0.10 g, 0.35 mmol), 4,4'-bipy-ethane (0.1 g, 0.6 mmol), and 10 mL of deionized water. The reaction was heated to 80 °C with constant stirring for 3 days, yielding yellow microcrystalline powder.

Synthesis of (4,4'-bipy-ethane)$_{0.5}$H$_x$WO$_3$

A 23 mL PTFE-lined Pressure vessel was loaded with $3Na_2WO_4{\cdot}9WO_3{\cdot}H_2O$ (0.3 g, 0.1 mmol), 4,4'-bipy-ethane (0.22 g, 1.2 mmol), W (0.030 g, 0.163 mmol), and 10 mL of deionized water. The PTFE-lined vessel was heated to 170 °C for 7 days, yielding black microcrystalline powder.

Synthesis of (4,4'-bpy-ethene)$_{0.5}$H$_x$MoO$_3$ (4,4'-bipy-ethene = 4,4′-vinylenedipyridine or 1,2-bis(4-pyridinyl)ethene)

A 20 mL vial was charged with MoO_3 (50 mg, 0.35 mmol), 4,4'-bipy-ethene (64 mg, 0.35 mmol), $Na_2S_2O_4$ (87 mg, 0.47 mmol), and 10 mL of deionized water, followed by heating to 80 °C with constant stirring for 5 days, yielding black microcrystalline powder.

Synthesis of (4,4'-bipy-ethene)$_{0.5}$WO$_3$

A 23 mL PTFE-lined pressure vessel was charged with $3Na_2WO_4{\cdot}9WO_3{\cdot}H_2O$ (0.10 g, 0.033 mmol), 4,4'-bipy-ethene (0.109 g, 0.598 mmol), and 6 mL of deionized water. The reaction was heated to 150 °C for 4 days, yielding golden microcrystalline powder. Alternatively, according to our stirring method, a 20 mL vial was charged with $WO_3{\cdot}H_2O$ (0.1 g, 0.4 mmol), 4,4'-bipy-ethene (0.109 g, 0.598 mmol), and 10 mL of deionized water. The reaction was heated to 80 °C with constant stirring for 3 days, yielding yellow microcrystalline powder.

Synthesis of (4,4'-bipy-ethene)$_{0.5}$H$_x$WO$_3$

A 23 mL PTFE-lined Pressure vessel with $3Na_2WO_4{\cdot}9WO_3{\cdot}H_2O$ (0.3 g, 0.1 mmol), 4,4'-bipy-ethene (0.220 g, 1.21 mmol), W (0.030 g, 0.16 mmol), and 10 mL of deionized water. The PTFE-lined vessel was heated to 170 °C for 7 days, yielding black microcrystalline powder.

Synthesis of (dps)$_{0.5}$WO$_3$ (dps = 4,4'-dipyridyl disulfide)

According to our mild method, $WO_3{\cdot}H_2O$ (0.1 g, 0.4 mmol), dps (44 mg, 0.20 mmol), and 10 mL of deionized water were combined in a 20 mL vial. The reaction was heated to 80 °C with constant stirring for 3 days, yielding dark yellow microcrystalline powder.

Synthesis of (4*H*-trz)$_{0.5}$MoO$_3$ (4*H*-trz = 4*H*-1,2,4-triazole)

A 20 mL vial was charged with MoO_3 (0.10 g, 0.69 mmol), 4*H*-trz (48 mg, 0.69 mmol), and 10 mL of deionized water. The reaction was heated to 80 °C with constant stirring for 24 hours. The product was also synthesized using $(NH_4)_6Mo_7O_{24}$ (0.116 g, 0.0996 mmol), 4*H*-trz (48 mg, 0.69 mmol), and 10 mL of

deionized water. The reaction was heated to 80 °C with constant stirring for 24 hours. Both synthetic methods yield white microcrystalline powder.

Synthesis of (4*H*-trz)$_{0.5}$H$_x$MoO$_3$

Multiple synthesis methods were used to obtain (4*H*-trz)$_{0.5}$H$_x$MoO$_3$. To acquire both single crystals and microcrystalline powders, a 23 mL PTFE-lined Pressure vessel was loaded with H$_{0.33}$MoO$_3$ (0.10 g, 0.69 mmol), 4*H*-trz (48 mg, 0.69 mmol), and 10 mL of deionized water. The PTFE-lined vessel was heated to 150 °C for 3 days, yielding black needle-shaped single crystals and microcrystalline powder. However, the single crystals were not of sufficient size for structure determination via single-crystal X-ray diffraction measurements. Reductions were also performed under milder stirring reactions. A 20 mL vial was charged with H$_{0.33}$MoO$_3$ (0.10 g, 0.69 mmol), 4*H*-trz (48 mg, 0.69 mmol), and 10 mL of deionized water. The reaction was heated to 80 °C with constant stirring for 3 days, yielding black microcrystalline powder. The same procedure wherein H$_{0.33}$MoO$_3$ is replaced with H$_{1.68}$MoO$_3$ (0.10 g, 0.69 mmol) yielded powder featuring a higher level of reduction. Alternatively, a 20 mL vial was charged with MoO$_3$ (0.050 g, 0.35 mmol), 4*H*-trz (24 mg, 0.35 mmol), Mo metal (either 5 mg [0.05 mmol] or 6 mg [0.06 mmol] to vary the reduction level), and 10 mL of deionized water. The reaction was heated to 80 °C with constant stirring for 3 days, yielding black microcrystalline powder. Alternatively, a 20 mL vial was charged with MoO$_3$ (0.050 g, 0.35 mmol), 4*H*-trz (24 mg, 0.35 mmol), Na$_2$S$_2$O$_4$ (87 mg, 0.50 mmol), and 10 mL of deionized water. The reaction was heated to 80 °C with constant stirring for 5 days, yielding black microcrystalline powder.

Synthesis of (4*H*-trz)$_{0.5}$WO$_3$[6]

A 20 mL vial was charged with 3Na$_2$WO$_4$·9WO$_3$·H$_2$O (0.10 g, 0.033 mmol), 4*H*-trz (41.6 g, 0.602 mmol), and 10 mL of deionized water. The reaction was heated to 80 °C with constant stirring for 5 days, yielding white microcrystalline powder.

Synthesis of (4*H*-trz)$_{0.5}$H$_x$WO$_3$

A 23 mL PTFE-lined Pressure vessel was charged with 3Na$_2$WO$_4$·9WO$_3$·H$_2$O (0.3 g, 0.1 mmol), 4*H*-trz (150 mg, 2.17 mmol), W metal (0.030 g, 0.16 mmol), and 10 mL of deionized water. The PTFE-lined vessel was heated to 170 °C for 7 days, yielding dark blue needle-shaped single crystals and microcrystalline powder. However, the single crystals were not of sufficient size for structure determination via single-crystal X-ray diffraction measurements. Alternatively, a 20 mL vial was charged with (4*H*-trz)$_{0.5}$WO$_3$ (25 mg, 0.094 mmol) and 5 mL of a 0.5 M aqueous solution of Na$_2$S$_2$O$_4$. The reaction mixture was allowed to stir under room temperature for 24 hours. A dark blue microcrystalline powder was isolated.

Synthesis of (py)WO$_3$[7] (py = pyridine)

A 20 mL vial was charged with 3Na$_2$WO$_4$·9WO$_3$·H$_2$O (0.10 g, 0.033 mmol), py (1.0 mL, 12 mmol), and 10 mL of deionized water. The reaction was heated to 80 °C with constant stirring for 5 days, yielding yellow microcrystalline powder.

Synthesis of (py)H$_x$WO$_3$

A 20 mL vial was charged with (py)WO$_3$ (25 mg, 0.080 mmol) and 5 mL of a 0.5 M aqueous solution of Na$_2$S$_2$O$_4$. The reaction mixture was allowed to stir under room temperature for 24 hours. A dark blue microcrystalline powder was isolated.

Synthesis of (py-4-vinyl)H_xMoO_3 (py-4-vinyl = 4-vinyl pyridine)

A 20 mL vial was charged with $H_{0.33}MoO_3$ (0.10 g, 0.69 mmol), py-4-vinyl (0.074 mL, 0.70 mmol), and 10 mL of deionized water. The reaction was heated to 100 °C with constant stirring for 5 days, yielding black microcrystalline powder.

Synthesis of (py-4-OH)MoO_3 (py-4-OH = 4-hydroxypyridine)

A 20 mL vial was charged with MoO_3 (0.100 g, 0.69 mmol), py-4-OH (33 mg, 0.35 mmol), and 10 mL of deionized water. The reaction was heated to 80 °C with constant stirring for 3 days, yielding white microcrystalline powder.

Crystal structure determination

Crystals were coated with Paratone-N oil, mounted on a Kapton® loop, and transferred to a Bruker D8 diffractometer equipped with a Bruker APEX-II detector. An arbitrary sphere of data was then collected using a combination of ω- and φ-scans of 0.5° with Mo Kα radiation (λ = 0.71073 Å).[8] Unit-cell parameters were refined against all data. The crystals did not show significant decay during data collection. Frames were integrated and corrected for Lorentz and polarization effects using SAINT 8.34a and were corrected for absorption effects using SADABS V2016.[9] Space-group assignment was based upon systematic absences, *E*-statistics, agreement factors for equivalent reflections, and successful refinement of the structure. The structure was solved through the intrinsic phasing method implemented in APEX4 and expanded routinely.[8,10-11] Solutions were refined against all data using the SHELXTL-2018 software package[11-13] and OLEX2.[10,12,14-15] Weighted *R* factors, R_w, and all goodness-of-fit indicators are based on F^2. Hydrogen atoms were inserted at idealized positions and refined using a riding model with an isotropic thermal parameter 1.2 times that of the attached carbon atom. Thermal parameters for non-hydrogen atoms were refined anisotropically, and in some cases, atoms were refined using a disorder model.

Powder X-ray diffraction (PXRD)

PXRD measurements were carried out on a Bruker D8 Advance diffractometer equipped with a Cu anode (Kα_1 = 1.54060 Å, Kα_2 = 1.54443 Å, Kα_2/Kα_1 = 0.50000), fixed divergence slits with a nickel filter, and a LYNXEYE detector. The instrument was operated in a Bragg-Brentano geometry with a step size of 0.01° or 0.02° 2θ. Le Bail refinements were performed in GSASII[16] by using modified single-crystal crystallographic information files (CIFs) of similar structures for which atoms were inserted or exchanged within OLEX2.[14] For example, by taking the CIF of $(azp)_{0.5}MoO_3$, Mo could be swapped for W to give the corresponding initial structural model for Le Bail refinement of $(azp)_{0.5}WO_3$. Likewise, carbon and hydrogen atoms could be readily substituted for the nitrogen atoms within the azo moiety to give the structural model for 4,4'-bipy-ethene-based materials. These models were then refined to fit experimental PXRD patterns. Chebyshev backgrounds were defined by manual point selection followed by fitting. The following parameters were then each individually allowed to refine, followed by simultaneous refinement of all parameters: scale factor, lattice parameters, peak-shape parameters according to a Thompson-Cox-Hastings pseudo-Voigt function, and finally intensities according to Le Bail. Atomic positions were not refined through Rietveld refinement due to the large number of atoms in the unit cell and data of insufficient resolution. However, these refinements indicate the successful isolation of several new hybrid phases, many of which we were able to successfully acquire single-crystal X-ray structures for their close structural analogs.

X-ray photoelectron spectroscopy (XPS)

Powder samples were mounted on a stainless-steel platen with double-sided carbon tape. X-ray photoelectron spectroscopy (XPS) was performed with a PHI VersaProbe II XPS instrument with a monochromatized Al Kα source under high vacuum (ca. 2×10^{-9} torr). Survey spectra were collected from 0 to 1100 eV using a step size of 0.8 eV at 50 ms/step and averaging 7 sweeps. High-resolution spectra were collected using a step size of 0.2 eV and averaging 20 sweeps. In some cases, an electron charge-compensation gun was used to prevent erroneous shifting of peaks due to sample charging. To ensure accurate comparisons across samples, the sp^2 carbon peak (set to 285 eV) was used for calibration. Peaks were fit according to a 30:70 Lorentzian:Gaussian ratio in CasaXPS after applying a Shirley background. To avoid overparameterization (i.e., overfitting), constraints were applied. First, the area ratios of spin-orbit split peaks were fixed according to ideal ratios, i.e., the Mo $3d_{3/2}$:$3d_{5/2}$ peak ratio was 2:3 and the W $4f_{5/2}$:$4f_{7/2}$ was 3:4. Second, it is generally not suggested to allow fwhm to freely vary without chemical reason,[17] therefore idealized fwhm were first determined by fitting fully oxidized Mo or W materials. A constraint of ±10% of this idealized value was then subsequently imposed in fitting of peaks in reduced congeners, where freely varying fwhm would lead to unstable fits due to the broad envelope resulting from combination of 6+, 5+, and 4+ oxidation states. In the case of W-based oxidized materials, the combination of high vacuum and charge compensation is known to reduce tungsten,[18] likely from creation of oxygen defects, leading to a small degree of W reduction (ca. 5%). Since the degree to which this effect occurs for already reduced tungsten-based oxide materials is not well-known, we incorporate the magnitude of this discrepancy as error in our calculated values of x in $(L)_zH_xWO_3$ (see Table 1 in the main text). On the other hand, more reduced hybrid bronzes may potentially undergo some surface reoxidation upon exposure to air and therefore the surface-sensitive nature of XPS may underestimate reduction levels. These errors are likely to cancel to some degree. XPS was used as the primary indicator of reduction level for materials discussed in the manuscript, since redox-titration has been shown to overestimate electron concentration in reduced metal oxide nanoparticles due to side reactions.[19]

Diffuse reflectance measurements

Diffuse reflectance spectra were acquired using a Jasco V-670 UV-Visible spectrophotometer outfitted with an integrating sphere. Microcrystalline sample powders were combined with $BaSO_4$ in a 1:10 ratio by weight and ground in a mortar and pestle to ensure homogeneity. Diffuse reflectance spectra were then collected after acquiring $BaSO_4$ background measurements and were transformed to pseudo-absorbance, α/S, according to the Kubelka-Munk equation[20] where α is the absorbance and S is the scattering coefficient. Oxidized and reduced forms of a given Mo or W material were normalized according to high energy absorption bands ca. 4.5 eV that are unaffected by reduction. Estimations of band gap energies were made using α/S vs. $h\nu$ pseudo-absorbance plots. Here, h is Planck's constant and ν is the frequency. The linear portion of the curve was then extrapolated, giving a band gap value, E_g. As mentioned in the text, due to the two-dimensional inorganic connectivity in these layered materials that gives rise to a two-dimensional density of states for their extended electronic structures, the Tauc method[21] that was originally developed for band gap determination of three dimensional semiconductors is not appropriate.

Conductivity measurements

Room temperature and variable temperature four-point resistance measurements were performed on cylindrical 6 or 13 mm pellets of microcrystalline sample that were pressed at 3000 or 11,000 pounds, respectively, for 30 minutes. Four steel wires were connected to the pellets in a van der Pauw configuration

with silver paint. Using a Bio-Logic SP300 or VSP3e potentiostat/galvanostat, measurements were acquired by obtaining current-voltage curves over a range of –20 to 20 mV or –40 to 40 mV at a scan rate of 5 $mV \cdot s^{-1}$ at each temperature. Voltage was measured across two adjacent leads while current was passed between the other two, per the van der Pauw method. Two resistance values are required to calculate the sheet resistance (R_s): a horizontal resistance R_h found by measuring voltage across the first and second leads, then a vertical resistance R_v from the voltage across the second and third leads (for example). Here, R_s (Ω) is given by the following equation:

$$e^{-\pi R_h/R_s} + e^{-\pi R_v/R_s} = 1$$

From R_s, one can then calculate resistivity, ρ (Ω·cm), by multiplying R_s by the thickness, t (cm). Data from all four possible configurations of R_h and R_v yielded the overall average resistivity (and therefore conductivity), with the standard deviation providing the error.

Variable temperatures in the range of 298 to 133 K during both cooling and warming were achieved by placing sample pellets within an Instec HCP621G-MPS cryostat chamber purged continuously with N_2. Measurements were acquired once the temperature was invariant.

Raman spectroscopy

Raman spectroscopy was performed on a Renishaw inVia confocal Raman microscope using 633 nm or 514.5 nm laser excitation lines at between 0.25–0.5 mW or 0.15–0.30 mW, respectively.

Infrared spectroscopy

Infrared spectra were collected on a Bruker Alpha II FT-IR spectrometer with attenuated total reflectance accessory.

Cyclic voltammetry

An electrode slurry was prepared using 16 mg of active material, 4 mg of Lib-SuperP conductive carbon, and 0.18 mL of a 5 wt% Nafion™ solution suspending in 18 mL of isopropanol, followed by ultrasonication overnight. 50 μL of this slurry were then deposited on a polished 7.07 mm^2 glassy carbon disc electrode and allowed to dry in air. Cyclic voltammetry was carried out using a three-electrode electrochemical cell with a Ag/AgCl reference electrode, Pt wire as a counter-electrode, and 1 M H_2SO_4 as the electrolyte. Standard voltametric measurements were then recorded using a Bio-Logic SP300 or VSP3e potentiostat/galvanostat.

Table S2. Crystallographic data[a] for $(azp)_{0.5}MoO_3$, $(pyz)_{0.5}H_{0.3}MoO_3$, and $(4,4'\text{-bipy})_{0.5}H_{0.3}WO_3$ at 120 K.

	$(azp)_{0.5}MoO_3$	**$(pyz)_{0.5}H_{0.3}MoO_3$[b]**	**$(4,4'\text{-bipy})_{0.5}H_{0.3}WO_3$[b]**
Empirical Formula	$C_5H_4N_2MoO_3$	$C_2H_2NMoO_3$	$C_5H_4NWO_3$
Formula Weight, g·mol^{-1}	236.04	183.99	309.94
Temperature, K	120	120	120
Crystal System	Orthorhombic	Tetragonal	Tetragonal
Space group	*Pbca*	*I4/mmm*	*I4/mmm*
a, Å	7.522(3)	5.2479(7)	5.2532(3)
b, Å	7.375(3)	5.2479(7)	5.2532(3)
c, Å	25.795(11)	14.143(3)	22.6462(16)
$\alpha = \beta = \gamma$, °	90	90	90
Volume, Å^3	1431.0(10)	389.50(13)	624.95(8)
Z	8	4	4
Density (calculated), g·cm^{-3}	2.191	3.138	3.294
Absorption coefficient, mm^{-1}	1.787	3.226	18.419
F(000)	912.0	348.0	556.0
Crystal size, mm^3	0.021 × 0.079 × 0.092	0.059 × 0.09 × 0.107	0.016 × 0.074 × 0.085
Crystal description	clear light orange plate	dark black block	clear dark yellow plate
θ range, °	3.159 to 26.360	2.881 to 28.236	1.798 to 28.281
Index ranges	$-9 \le h \le 9$ $-9 \le k \le 9$ $-31 \le l \le 31$	$-6 \le h \le 6$ $-6 \le k \le 6$ $-18 \le l \le 18$	$-7 \le h \le 6$ $-7 \le k \le 6$ $-30 \le l \le 30$
Reflections collected/unique	15450/1402	2961/173	7816/272
Completeness to θ_{max}, %	99.9	98.9	99.6
Max. and min. transmission	0.808, 0.958	0.799, 0.837	0.428, 0.604
Data/parameters/restraints	1402/95/12	173/21/0	27/30/0
Goodness-of-fit on F^2	1.211	1.390	1.229
Final *R* indices [$I > 2\sigma(I)$][b]	$R_1 = 0.0814$ w$R_2 = 0.1693$	$R_1 = 0.0181$ w$R_2 = 0.0556$	$R_1 = 0.0128$ w$R_2 = 0.0323$
R indices (all data)[c]	$R_1 = 0.0969$ w$R_2 = 0.1753$	$R_1 = 0.0185$ w$R_2 = 0.0559$	$R_1 = 0.016$ w$R_2 = 0.0327$
Largest diff. peak and hole, e·Å^{-3}	4.363, –4.043	0.595, –1.619	1.258, –1.290

[a]Obtained with $\lambda = 0.71073$ Å radiation

[b]Reduction values, i.e., *x* in $(L)_{0.5}H_xMO_3$ were not determined crystallographically and therefore are not included in the formulas of this table. These values are determined by XPS.

[c]$R_1 = \Sigma||F_o| - |F_c||/\Sigma|F_o|$, w$R_2 = [\Sigma w(F_o^2 - F_c^2)^2/\Sigma(F_o^2)^2]^{1/2}$

Table S3. Structural information derived from Le Bail fits of powder X-ray diffraction data.[a]

	(4*H*-trz)$_{0.5}$H$_{0.09}$MoO$_3$[b]	**(azp)$_{0.5}$WO$_3$**	**(4,4'-bipy-ethene)$_{0.5}$WO$_3$**	**(4,4'-bipy-ethene)$_{0.5}$H$_{0.3}$WO$_3$**[b]
Formula	$C_2H_3N_2Mo_2O_6$	$C_5H_4N_2WO_3$	$C_6H_5NWO_3$	$C_6H_5NWO_3$
Structure modified for Le Bail refinement[b]	(4*H*-trz)$_{0.5}$MoO$_3$	(azp)$_{0.5}$MoO$_3$	(azp)$_{0.5}$MoO$_3$	(4,4'-bipy-ethene)$_{0.5}$WO$_3$
Crystal System	Orthorhombic	Orthorhombic	Monoclinic	Monoclinic
Space group	*Pbcm*	*Pbca*	*P2$_1$/c*	*P2$_1$/c*
a, Å	3.80533(12)	7.4938(8)	7.3679(7)	7.3376(15)
b, Å	14.2083(5)	7.4260(6)	7.7497(12)	7.7102(14)
c, Å	13.4807(5)	26.238(3)	26.9309(18)	26.962(6)
α, β, γ (°)	90, 90, 90	90, 90, 90	90, 91.048(17), 90	90, 91.42(4), 90
Volume, Å^3	728.87(3)	1460.13(29)	1537.48(26)	1524.9(6)
R value (%)	6.13	8.02	11.33	17.74

[a]Obtained with λ = 1.5406 Å radiation

[b]Reduction values, i.e., *x* in (L)$_{0.5}$H$_x$MO$_3$ were not determined crystallographically and therefore are not included in the formulas of this table. These values are determined by XPS.

Table S4. Bond-valence sum calculations derived from single-crystal X-ray structures.[a]

Material	Bond	Bond Lengths (Å)	Bond-Valence Sum
(4,4'-bipy)$_{0.5}$MoO$_3$ [4]	μ_1-Mo$_1$–O	1.696(5)	6.03(2)
	μ_2-Mo$_1$–O	1.764(5), 1.810(5), 2.006(5), 2.120(5)	
	Mo$_1$–N	2.411(7)	
	μ_1-Mo$_2$–O	1.700(5)	
	μ_2-Mo$_2$–O	1.763(5), 1.829(5), 1.965(5), 2.120(5)	
	Mo$_2$–N	2.413(7)	
(4,4'-bipy)$_{0.5}$H$_x$MoO$_3$ [4]	μ_1-Mo$_1$–O	1.689(5)	5.63(1)
	μ_2-Mo$_1$–O	1.927(6), 1.927(6), 1.927(6), 1.927(6)	
	Mo$_1$–N	2.446(5)	
(pyz)$_{0.5}$H$_{0.3}$MoO$_3$ (this work)	μ_1-Mo$_1$–O	1.682(5)	5.725(8)
	μ_2-Mo$_1$–O	1.9205(9), 1.9205(9), 1.9205(9), 1.9205(9)	
	Mo$_1$–N	2.469(6)	
(azp)$_{0.5}$MoO$_3$ (this work)	μ_1-Mo$_1$–O	1.692(9)	6.36(24)[b]
	μ_2-Mo$_1$–O	1.74(1), 1.78(1), 2.01(1), 2.09(1)	
	Mo$_1$–N	2.42(1)	

[a]Bond valence sums were calculated according to reported methods.[22-23] Oxidation-state-independent values of tabulated bond lengths, R_0, and the empirical parameters, *b*, for molybdenum[24] were derived from the bvparm202.cif file maintained by the IUCr at https://www.iucr.org/resources/data/datasets/bond-valence-parameters. Calculations are shown for each crystallographically unique metal center.

[b]The (azp)$_{0.5}$MoO$_3$ structure is of somewhat lower resolution, and it is likely that the error on this BVS value is higher than the apparent propagated error from the measured bond lengths. This sample is fully oxidized based on optical measurements and cyclic voltammetry.

Table S5. Band gap values derived from diffuse reflectance spectra of hybrid and inorganic metal oxides (Figs. S29–S30). Errors are determined based on standard error of intercept and slope parameters from fits.

Material	Band Gap (eV)
$(4,4'\text{-bipy})_{0.5}MoO_3$	2.41(5)
$(azp)_{0.5}MoO_3$	2.38(1)
$(4H\text{-trz})_{0.5}MoO_3$	2.93(1)
$(py\text{-}4\text{-}OH)_{0.5}MoO_3$	3.49(4)
$(4,4'\text{-bipy})_{0.5}WO_3$	2.46(8)
$(azp)_{0.5}WO_3$	2.55(1)
$(pyz)_{0.5}WO_3$	2.27(2)
$(4,4'\text{-bipy-ethene})_{0.5}WO_3$	2.47(1)
$(4,4'\text{-bipy-ethane})_{0.5}WO_3$	2.41(6)
$(4H\text{-trz})_{0.5}WO_3$	2.88(1)
$(py)WO_3$	2.40(2)
MoO_3	2.86
WO_3	2.69

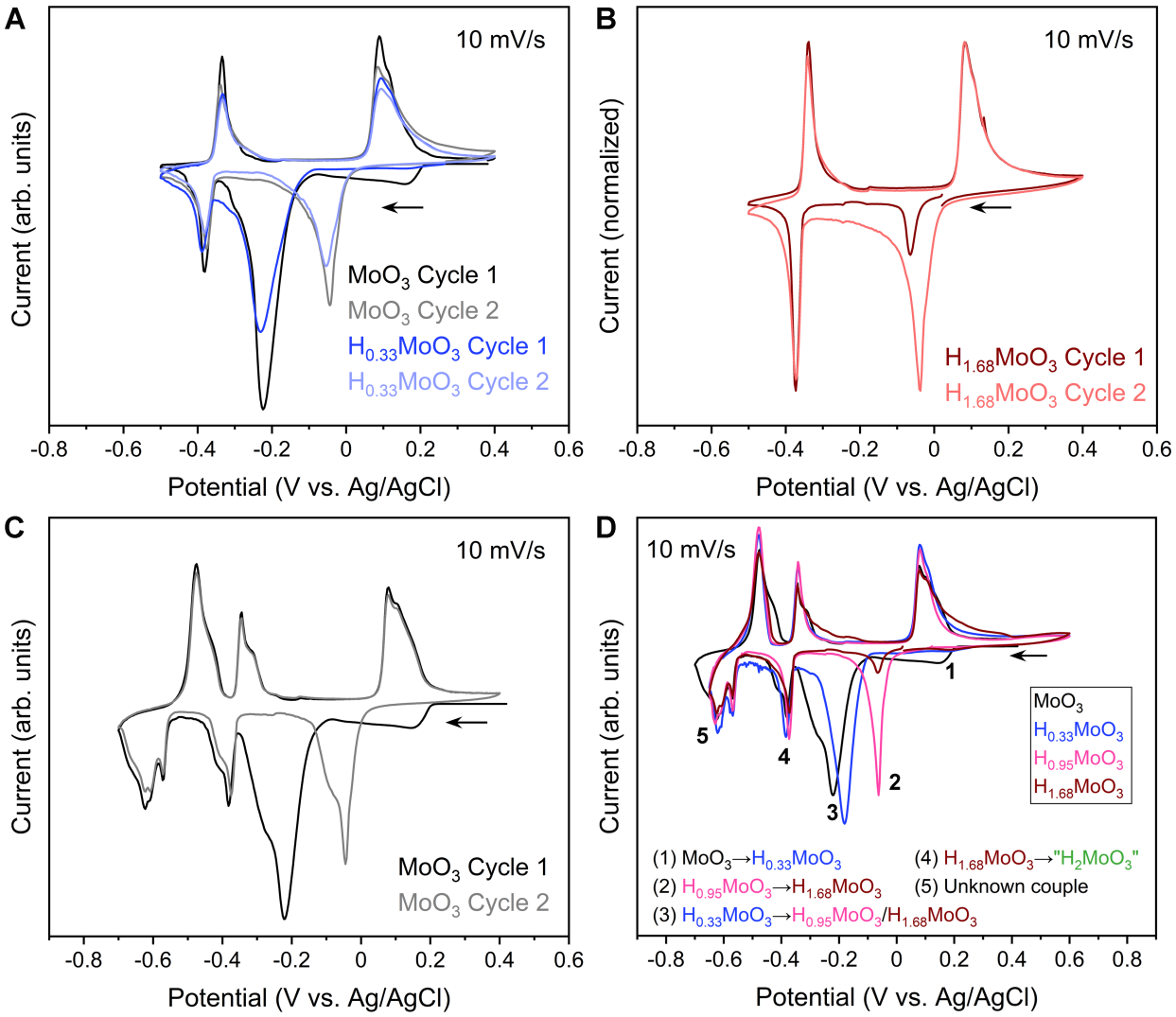

Figure S1. Cyclic voltammograms for MoO_3 and its reduced phases acquired in 1 M H_2SO_4. **A**) Comparison of the first two cycles for MoO_3 (gray scale) and $H_{0.33}MoO_3$ (blue scale); the arrow indicates the direction of initial scan. In both cases, there is a large, irreversible reduction at ca. -0.2 V vs. Ag/AgCl on the first cycle. On the second cycle, the reduction at ca. 0.05 V appears and is stable in further cycling. It is quasi-reversibly coupled with the oxidation at 0.1 V. Therefore, the key difference is in another reductive wave observed at 0.2 V for MoO_3 but not for $H_{0.33}MoO_3$. **B**) Comparison of the first two cycles for $H_{1.68}MoO_3$, showing that the sharp reductive peak ca. 0.05 V vs. Ag/AgCl is minimal on the first cycle but much larger on the second cycle after the material has been reoxidized. The small peak at 0.05 V on the first cycle is likely a small impurity of $H_{0.95}MoO_3$. **C**) Comparison of the first and second cycles for MoO_3 over a wider scan range showing another, unknown quasi-reversible redox couple with a multi-peak reduction centered at −0.6 V vs. Ag/AgCl and its corresponding oxidation peak at −0.5 V. **D**) Summary figure comparing the behavior of MoO_3, $H_{0.33}MoO_3$, $H_{0.95}MoO_3$, and $H_{1.68}MoO_3$. Numbers label specific, assigned reduction events. In order, reduction **1** corresponds to conversion of MoO_3 to $H_{0.33}MoO_3$ as determined by the scans in **A** and **C**. Reduction **2** corresponds to the conversion of $H_{0.95}MoO_3$ to $H_{1.68}MoO_3$ as determined by the scans in **B**. Reduction peak **3** corresponds to the irreversible, concerted conversion of $H_{0.33}MoO_3$ to $H_{0.95}MoO_3$ and $H_{1.68}MoO_3$, as determined by scans in **A**, **B**, and **C**. Reduction **4** corresponds to the conversion of $H_{1.68}MoO_3$ to H_2MoO_3 as determined by the scans in **B**. Finally, reduction **5** is an unknown redox couple that is nevertheless relatively stable to cycling. These assignments agree with recent electrochemical reports[25] as well as prior synthetic reports.[1,26]

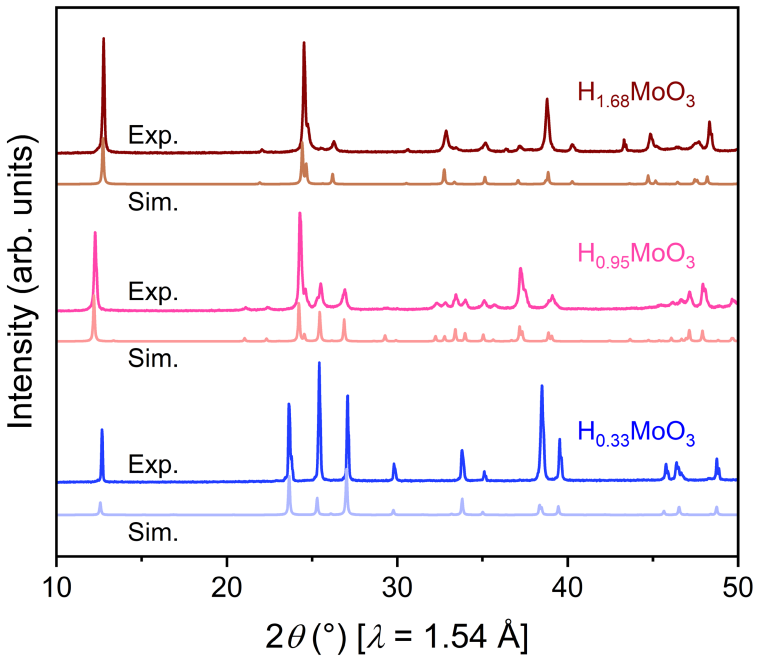

Figure S2. Powder X-ray diffraction (PXRD) patterns for the hydrogen molybdenum bronzes H_xMoO_3 (x = 0.33, 0.95, 1.68). Experimental (Exp.) patterns are compared to simulated (Sim.) patterns generated based on reported crystallographic information files from the Inorganic Crystal Structure Database (ICSD; FIZ Karlsruhe).

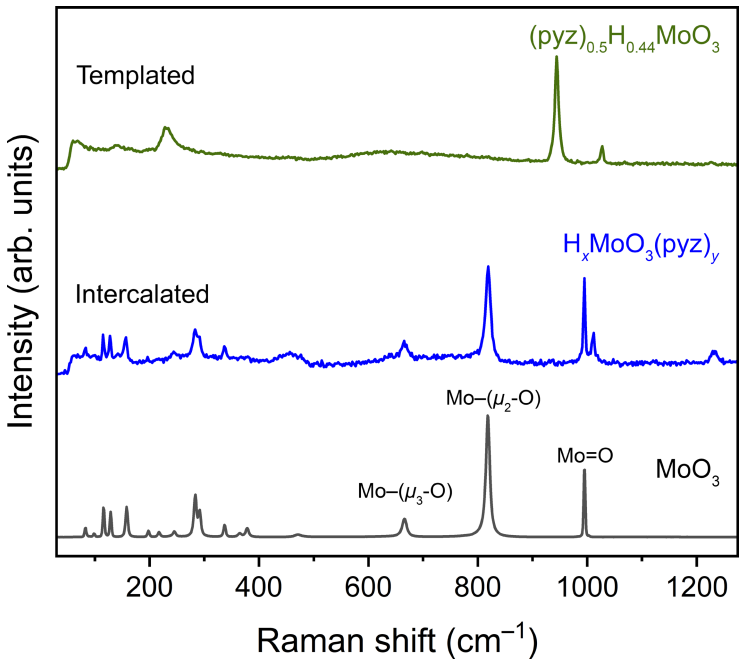

Figure S3. Raman spectra for MoO_3, $H_xMoO_3(pyz)_y$ (a representative intercalated sample), and $(pyz)_{0.5}H_{0.44}MoO_3$ (a representative templated structure). Modes at 665 cm^{-1}, 820 cm^{-1}, and 995 cm^{-1} in $H_xMoO_3(pyz)_y$ are virtually identical to modes in MoO_3 assigned to metal bonding to bridging μ_3-oxos, bridging μ_2-oxos, and terminal μ_1-oxos, respectively. For the templated structure, the broader feature ca. 600 cm^{-1} is attributed to bridging μ_2-oxo modes while the higher-energy feature ca. 940 cm^{-1} is assigned to a terminal metal-oxo.

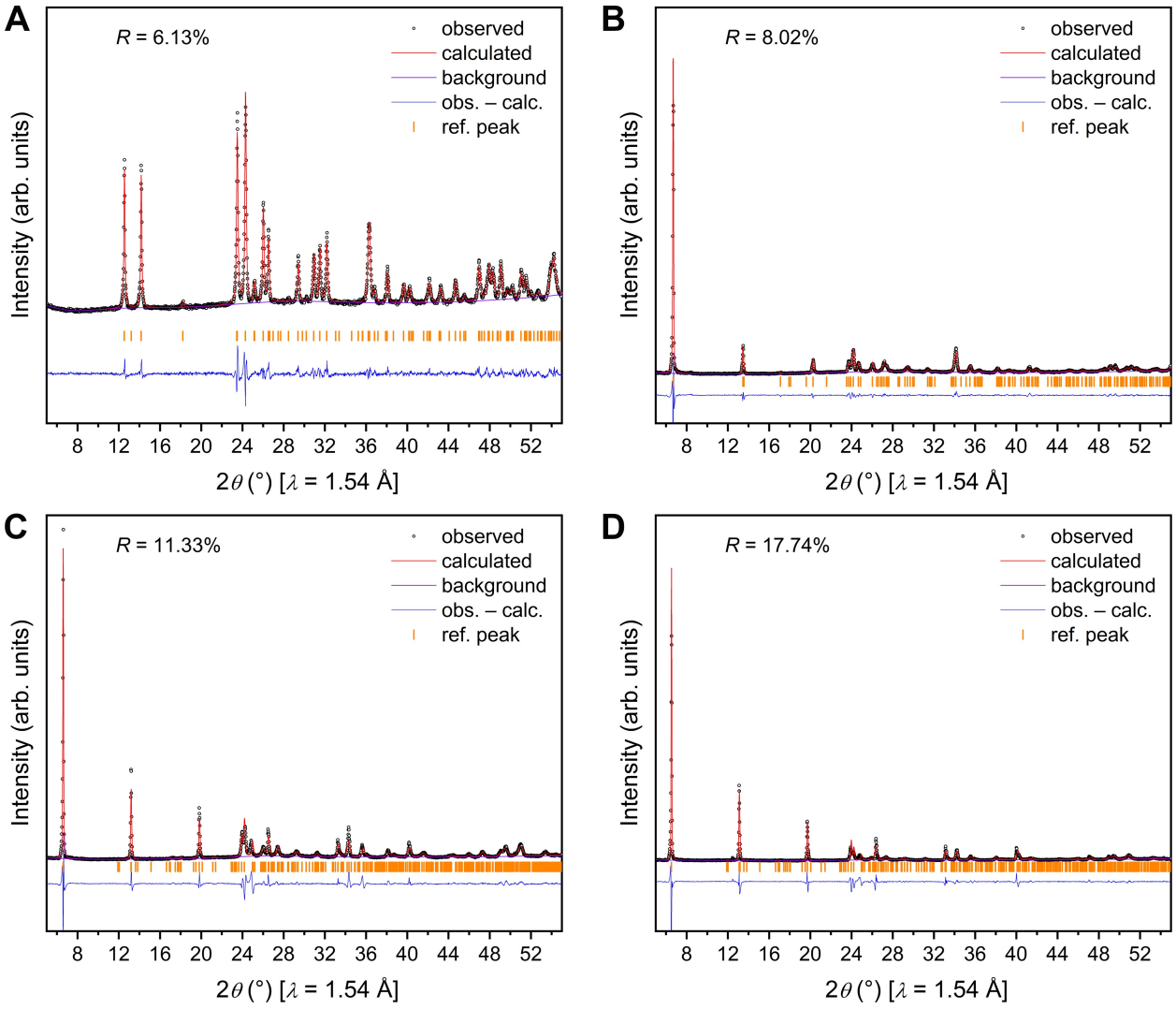

Figure S4. Le Bail refinements of powder X-ray diffraction (PXRD) patterns for **A**) (4*H*-trz)$_{0.5}$H$_{0.09}$MoO$_3$, **B**) (azp)$_{0.5}$WO$_3$, **C**) (4,4'-bipy-ethene)$_{0.5}$WO$_3$, and **D**) (4,4'-bipy-ethene)$_{0.5}$H$_{0.3}$WO$_3$. Per the Le Bail method, only lattice constants and peak shapes were refined, leaving atomic positions fixed. We find the agreement sufficient for evidence of pure phase isolation and to corroborate atomic coordinates of atoms in unit cell.

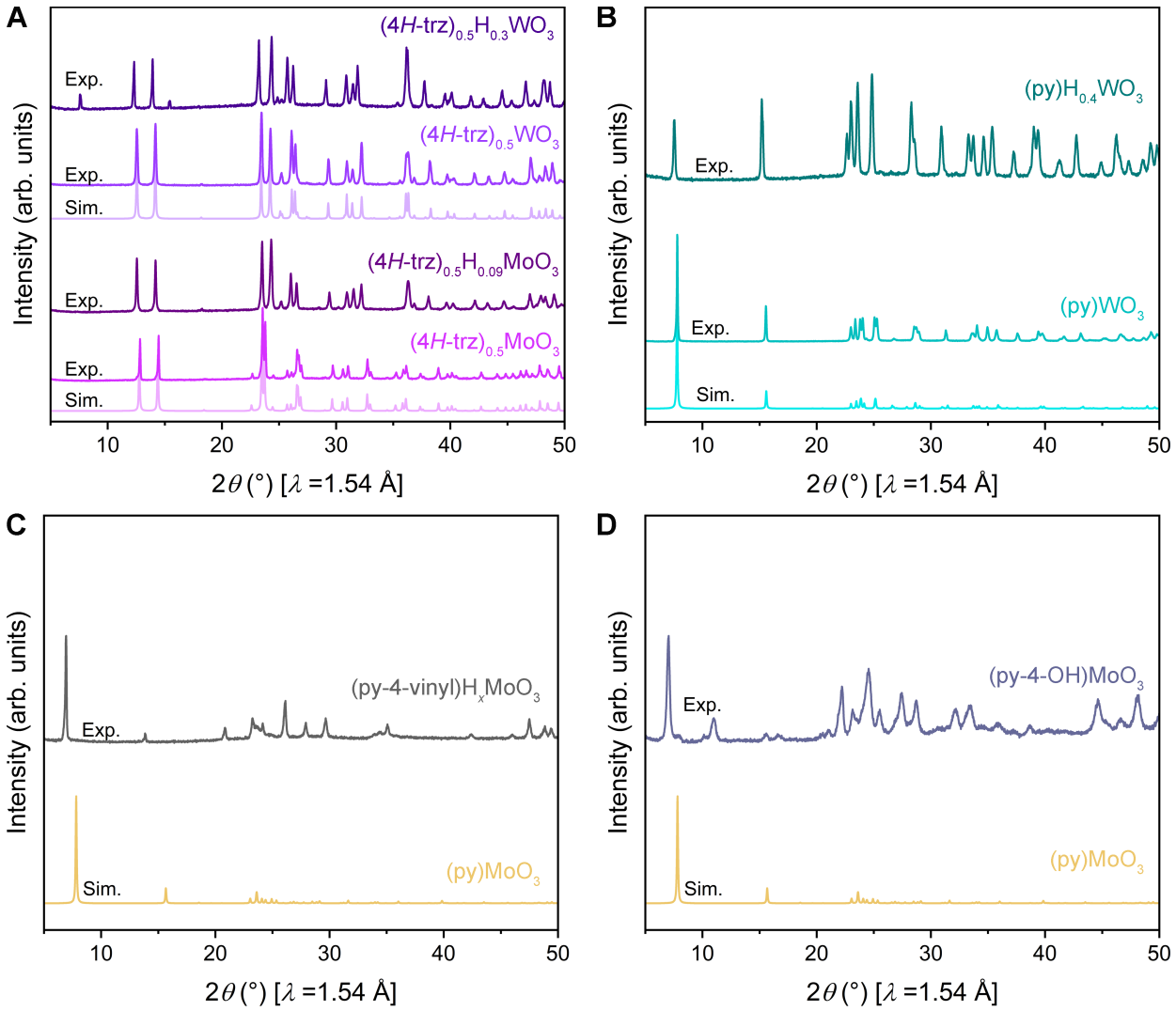

Figure S5. Powder X-ray diffraction (PXRD) patterns for hybrid bronzes and their oxidized congeners in which the organic ligands do not pillar the inorganic layers, i.e., these are bilayered materials. Experimental (Exp.) patterns are compared to simulated (Sim.) patterns generated from single-crystal structures. **A**) $(4H\text{-trz})_{0.5}H_xMoO_3$ (x = 0, 0.09) and $(4H\text{-trz})_{0.5}H_xWO_3$ (x = 0, 0.3). **B**) $(py)H_xWO_3$ (x = 0, 0.4). **C**) (py-4-vinyl)$H_x$$MoO_3$ shown in comparison to the simulated pattern for $(py)MoO_3$. **D**) (py-4-OH)MoO_3 shown in comparison to the simulated pattern for $(py)MoO_3$.

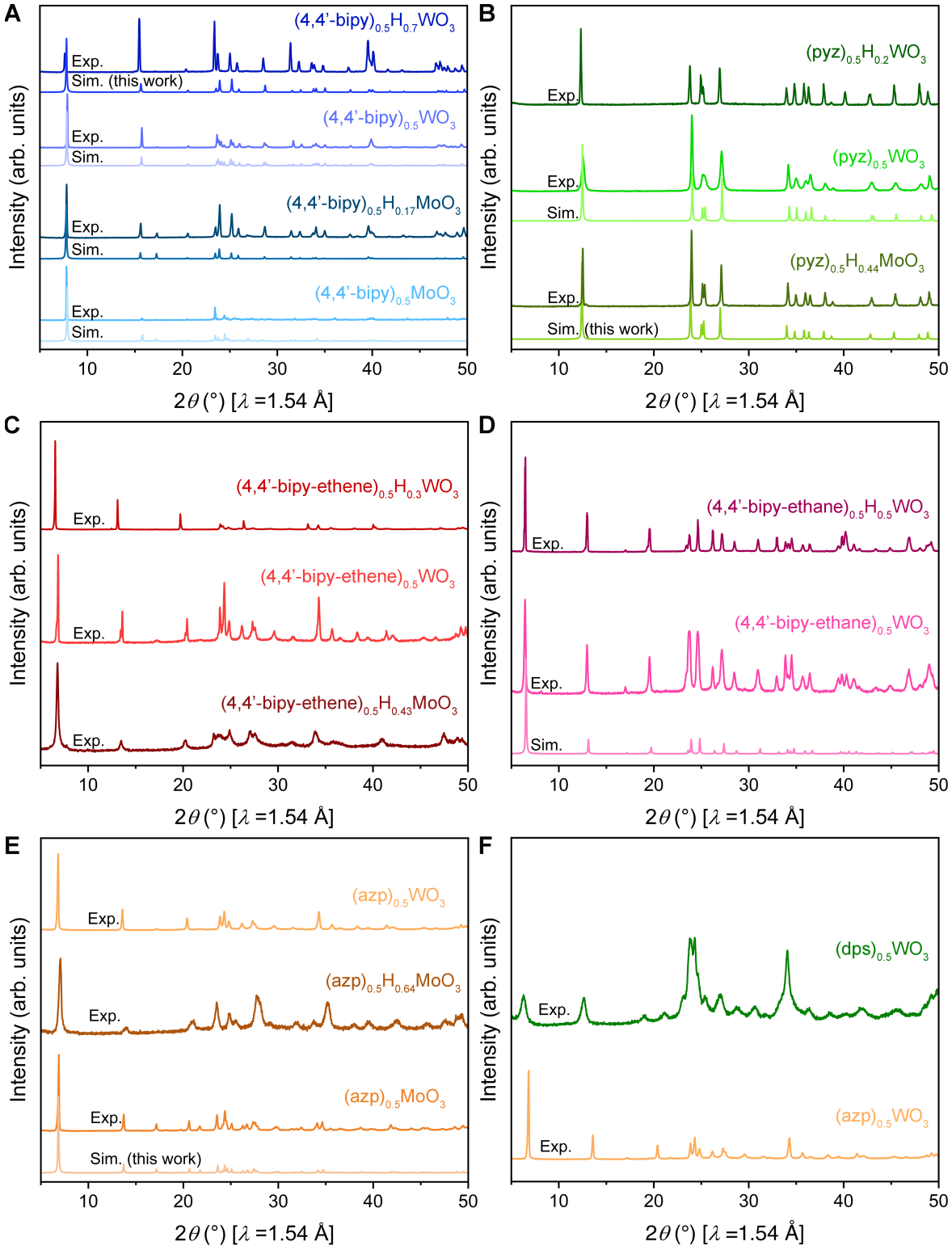

Figure S6. Powder X-ray diffraction (PXRD) patterns for hybrid bronzes and their oxidized congeners in which the organic ligands pillar the inorganic layers. Experimental (Exp.) patterns are compared to simulated (Sim.) patterns generated from single-crystal structures. **A**) (4,4'-bipy)$_{0.5}$H$_x$MoO$_3$ (x = 0, 0.17) and (4,4'-bipy)$_{0.5}$H$_x$WO$_3$ (x = 0, 0.7). **B**) (pyz)$_{0.5}$H$_x$WO$_3$ (x = 0, 0.2) and (pyz)$_{0.5}$H$_{0.44}$MoO$_3$. **C**) (4,4'-bipy-ethene)$_{0.5}$H$_x$WO$_3$ (x = 0, 0.3) and (4,4'-bipy-ethene)$_{0.5}$H$_{0.43}$MoO$_3$. **D**) (4,4'-bipy-ethane)$_{0.5}$H$_x$WO$_3$ (x = 0, 0.5). **E**) (azp)$_{0.5}$H$_x$MoO$_3$ (x = 0, 0.64) and (azp)$_{0.5}$WO$_3$. **F**) (dps)$_{0.5}$WO$_3$ shown in comparison to the experimental pattern for (azp)$_{0.5}$WO$_3$.

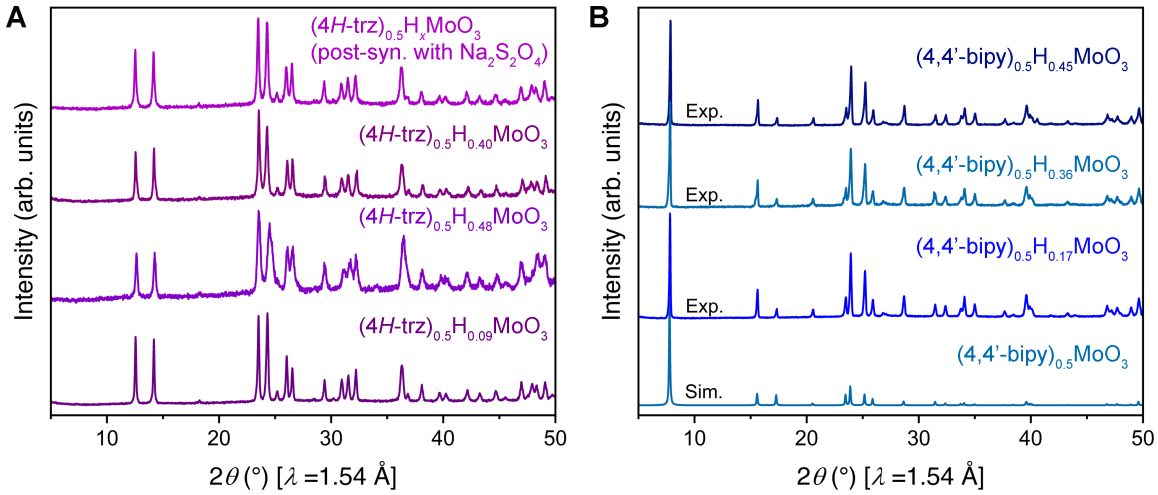

Figure S7. Powder X-ray diffraction (PXRD) patterns for representative materials showing that method or level of reduction do not significantly impact symmetry, lattice constants, or crystallinity. **A**) $(4H\text{-trz})_{0.5}H_xMoO_3$ with $x = 0.09$ ($H_{0.33}MoO_3$ as a starting material), $x = 0.48$ ($H_{1.68}MoO_3$ as a starting material), $x = 0.40$ (*in situ* reduction with Mo metal), and post-synthetically reduced with $Na_2S_2O_4$. **B**) $(4,4'\text{-bipy})_{0.5}H_xMoO_3$ with $x = 0.17$ ($H_{0.33}MoO_3$ as a starting material), $x = 0.36$ ($H_{1.68}MoO_3$ as a starting material), and $x = 0.45$ (*in situ* reduction with Mo metal). Many additional materials were synthesized in this manner as well (see experimental methods above and Table 1 in the manuscript).

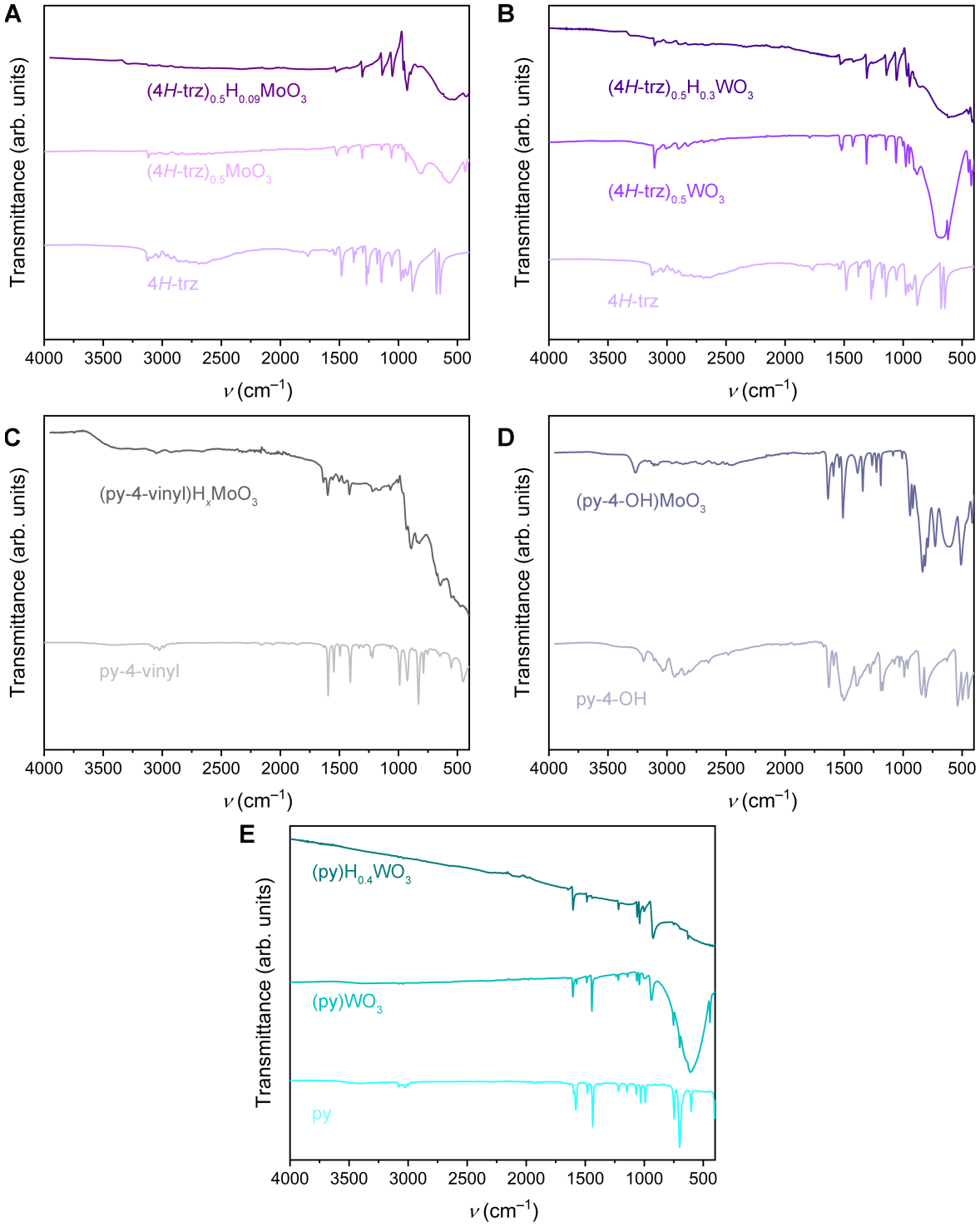

Figure S8. FT-IR spectra for bilayered hybrid metal oxides and their reduced hybrid bronze analogs shown in comparison to their corresponding organic ligands. Shifts of ligand-derived peaks in the hybrid materials corroborate their binding. The reduced hybrid bronzes show increased broad absorption relative to the oxidized forms that monotonically increases with decreasing wavenumber. No discernible IVCT/polaronic peak is observed. **A**) (4*H*-trz)$_{0.5}$H$_x$MoO$_3$ (x = 0, 0.09). **B**) (4*H*-trz)$_{0.5}$H$_x$WO$_3$ (x = 0, 0.3). **C**) (py-4-vinyl)H$_x$MoO$_3$. **D**) (py-4-OH)MoO$_3$. **E**) (py)H$_x$WO$_3$ (x = 0, 0.4).

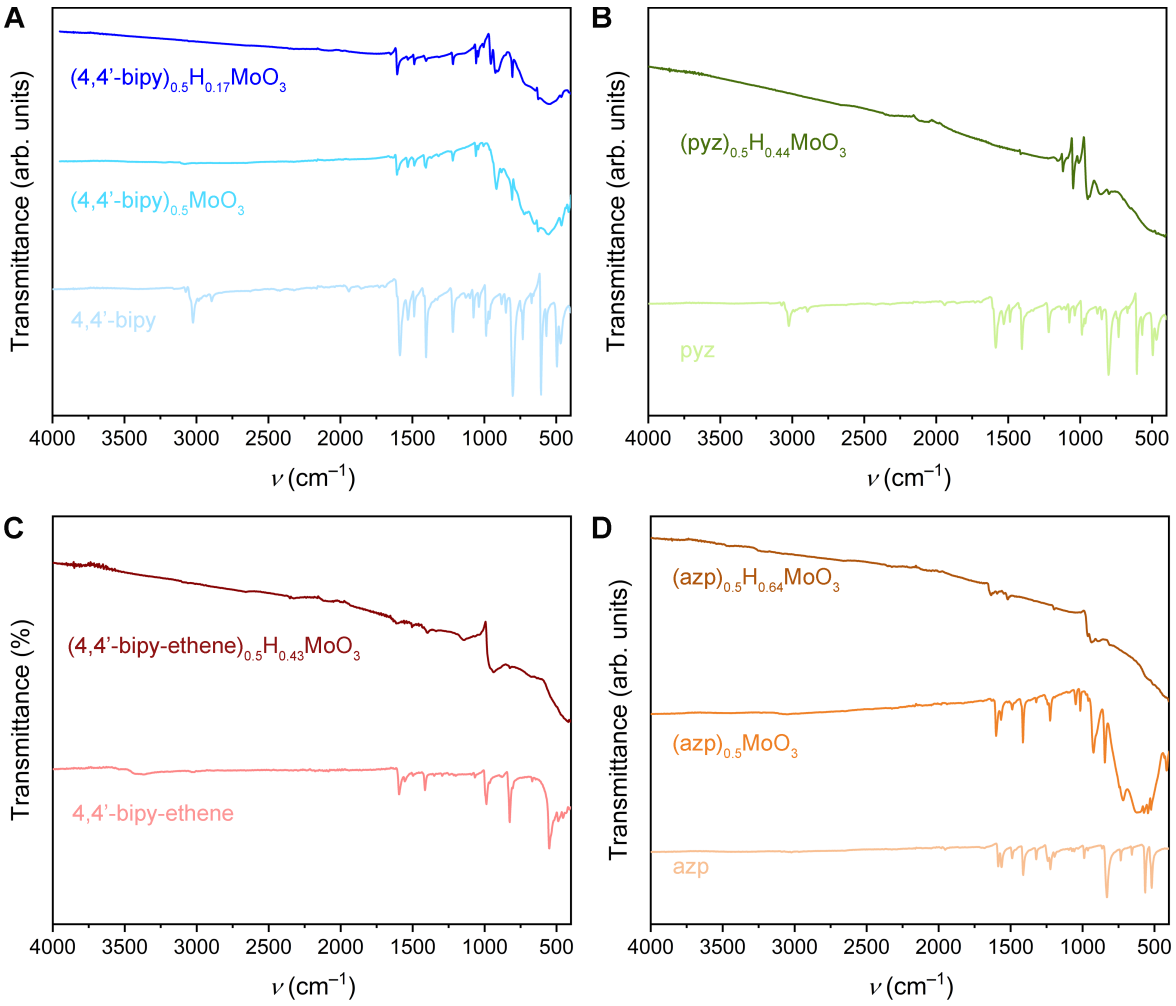

Figure S9. FT-IR spectra for pillared hybrid molybdenum oxides and their reduced hybrid bronze analogs shown in comparison to their corresponding organic ligands. Shifts of ligand-derived peaks in the hybrid materials corroborate their binding. The reduced hybrid bronzes show increased broad absorption relative to the oxidized forms that monotonically increases with decreasing wavenumber. No discernible IVCT/polaronic peak is observed. **A**) (4,4'-bipy)$_{0.5}$H$_x$MoO$_3$ (x = 0, 0.17). **B**) (pyz)$_{0.5}$H$_{0.44}$MoO$_3$. **C**) (4,4'-bipy-ethene)$_{0.5}$H$_{0.43}$MoO$_3$. **D**) (azp)$_{0.5}$H$_x$MoO$_3$ (x = 0, 0.64).

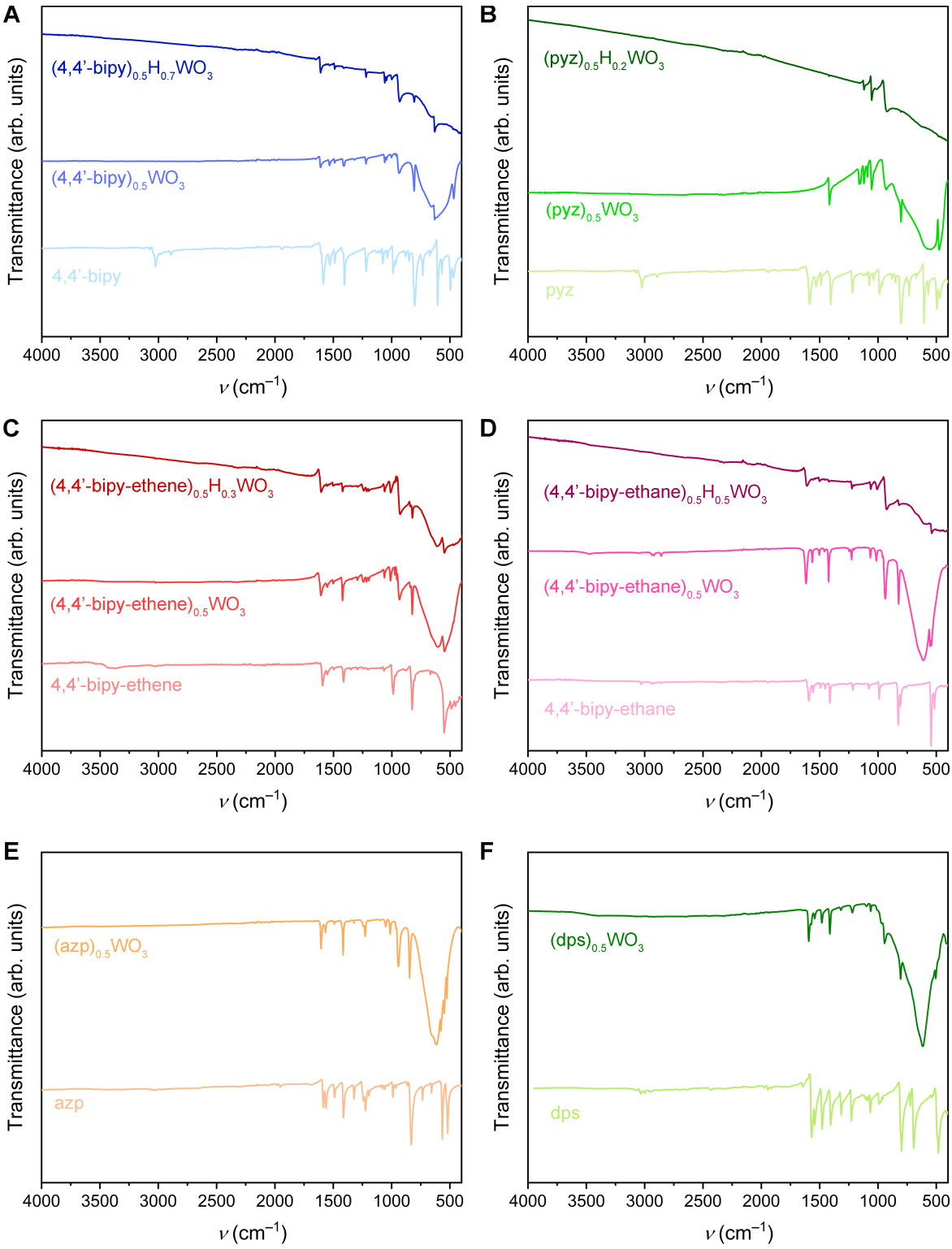

Figure S10. FT-IR spectra for pillared hybrid tungsten oxides and their reduced hybrid bronze analogs shown in comparison to their corresponding organic ligands. Shifts of ligand-derived peaks in the hybrid materials corroborate their binding. The reduced hybrid bronzes show increased broad absorption relative to the oxidized forms that monotonically increases with decreasing wavenumber. No discernible IVCT/polaronic peak is observed. **A**) (4,4'-bipy)$_{0.5}$H$_x$WO$_3$ (x = 0, 0.7). **B**) (pyz)$_{0.5}$H$_x$WO$_3$ (x = 0, 0.2). **C**) (4,4'-bipy-ethene)$_{0.5}$H$_x$WO$_3$ (x = 0, 0.3). **D**) (4,4'-bipy-ethane)$_{0.5}$H$_x$WO$_3$ (x = 0, 0.5). **E**) (azp)$_{0.5}$WO$_3$. **F**) (dps)$_{0.5}$WO$_3$.

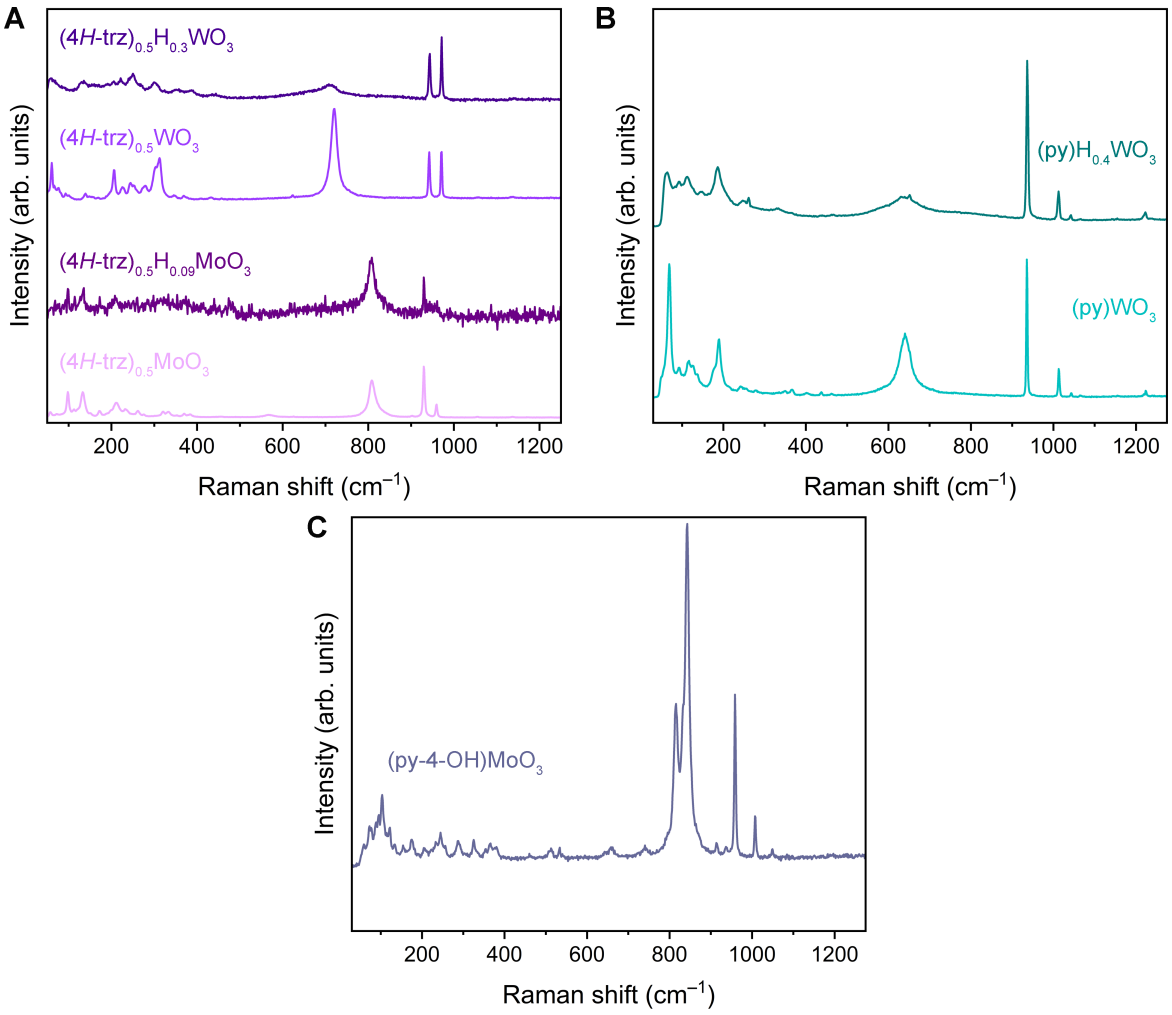

Figure S11. Raman spectra for bilayered hybrid metal oxides and their reduced hybrid bronze analogs. The reduced hybrid bronzes show low intensity and weak features due to increased absorption of the laser and/or enhanced scattering. In some cases, the laser absorption was so prevalent that no discernible peaks were observed. The broader features between 600–850 cm^{-1} are attributed to O–M–O modes while higher-energy features between 900–1000 cm^{-1} are assigned to terminal metal-oxos. **A**) $(4H\text{-trz})_{0.5}H_xMoO_3$ (x = 0, 0.09) and $(4H\text{-trz})_{0.5}H_xWO_3$ (x = 0, 0.3). **B**) $(py)H_xWO_3$ (x = 0, 0.4). **C**) (py-4-OH)MoO_3.

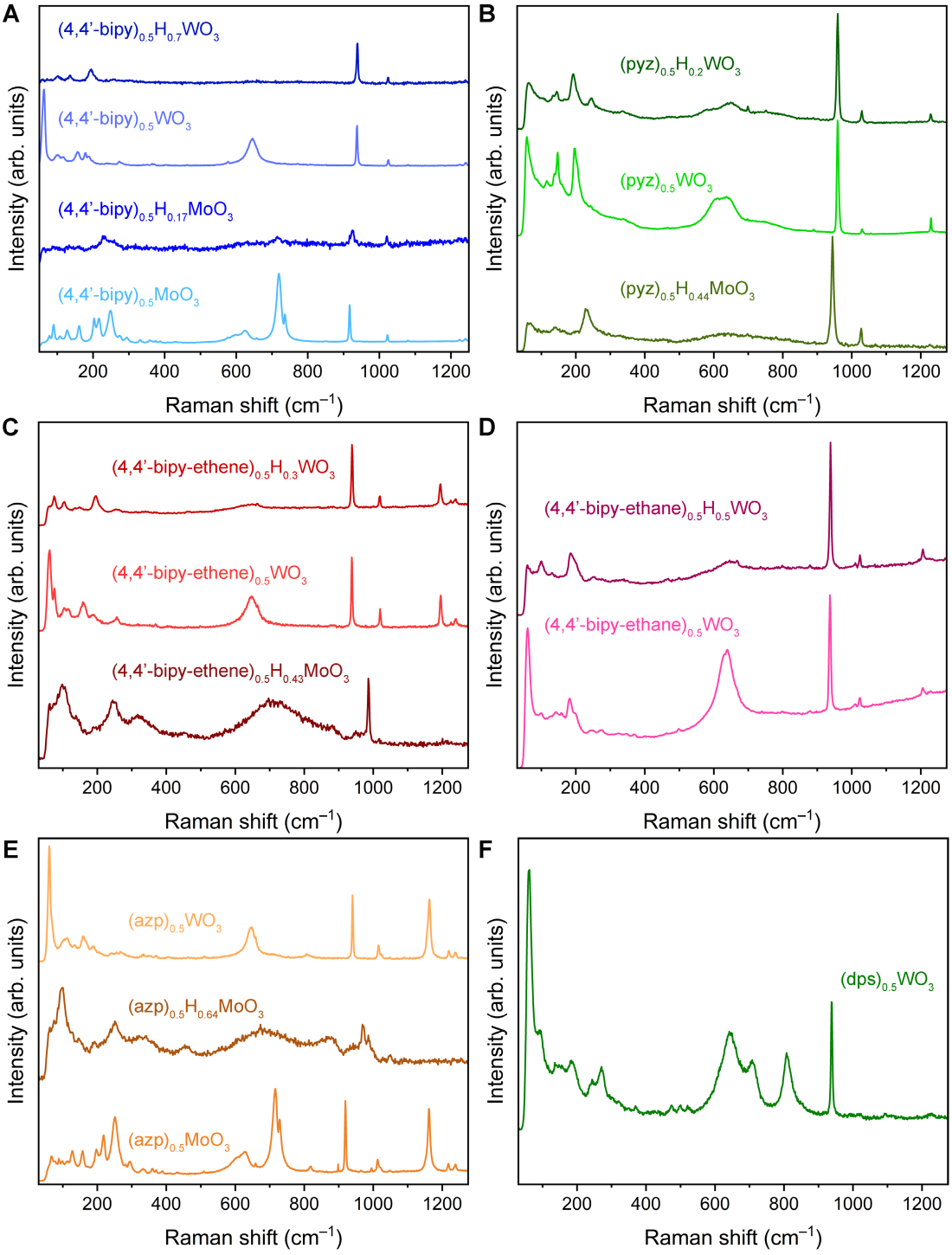

Figure S12. Raman spectra for pillared hybrid metal oxides and their reduced hybrid bronze analogs. The reduced hybrid bronzes show low intensity and weak features due to increased absorption of the laser and/or enhanced scattering. In some cases, the laser absorption was so prevalent that no discernible peaks were observed. The broader features between 600–850 cm^{-1} are attributed to O–M–O modes while higher-energy features between 900–1000 cm^{-1} are assigned to terminal metal-oxos. **A**) (4,4'-bipy)$_{0.5}$H$_x$MoO$_3$ (x = 0, 0.17) and (4,4'-bipy)$_{0.5}$H$_x$WO$_3$ (x = 0, 0.7). **B**) (pyz)$_{0.5}$H$_x$WO$_3$ (x = 0, 0.2) and (pyz)$_{0.5}$H$_{0.44}$MoO$_3$. **C**) (4,4'-bipy-ethene)$_{0.5}$H$_x$WO$_3$ (x = 0, 0.3) and (4,4'-bipy-ethene)$_{0.5}$H$_{0.43}$MoO$_3$. **D**) (4,4'-bipy-ethane)$_{0.5}$H$_x$WO$_3$ (x = 0, 0.5). **E**) (azp)$_{0.5}$H$_x$MoO$_3$ (x = 0, 0.64) and (azp)$_{0.5}$WO$_3$. **F**) (dps)$_{0.5}$WO$_3$.

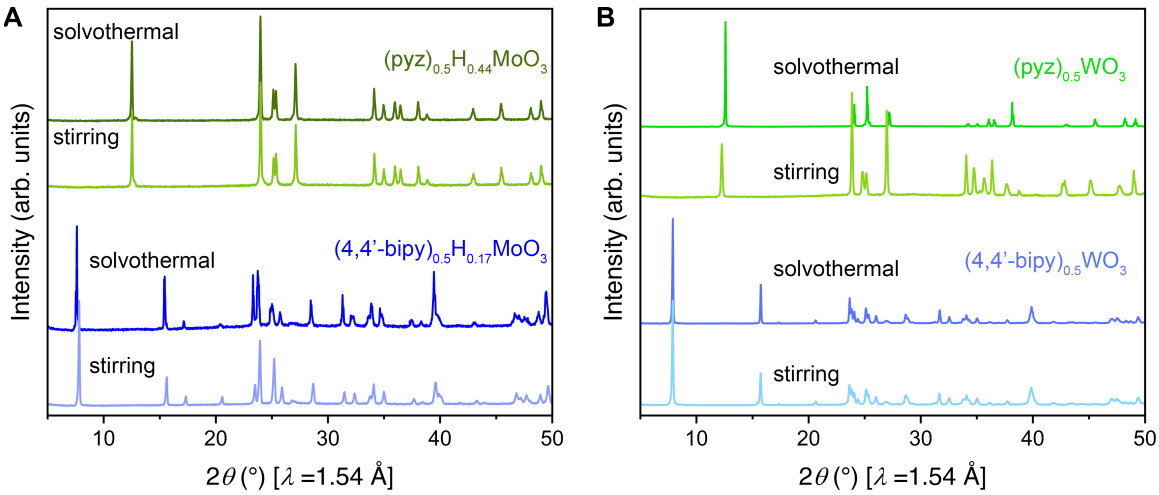

Figure S13. Powder X-ray diffraction (PXRD) patterns for representative **A**) molybdenum- and **B**) tungsten-based hybrids comparing their syntheses via solvothermal and mild solution-state stirring reactions. In the latter, high crystallinity is still retained despite the shorter reaction times and lower temperatures. Many additional materials were synthesized in this manner as well (see Table 1 in the manuscript).

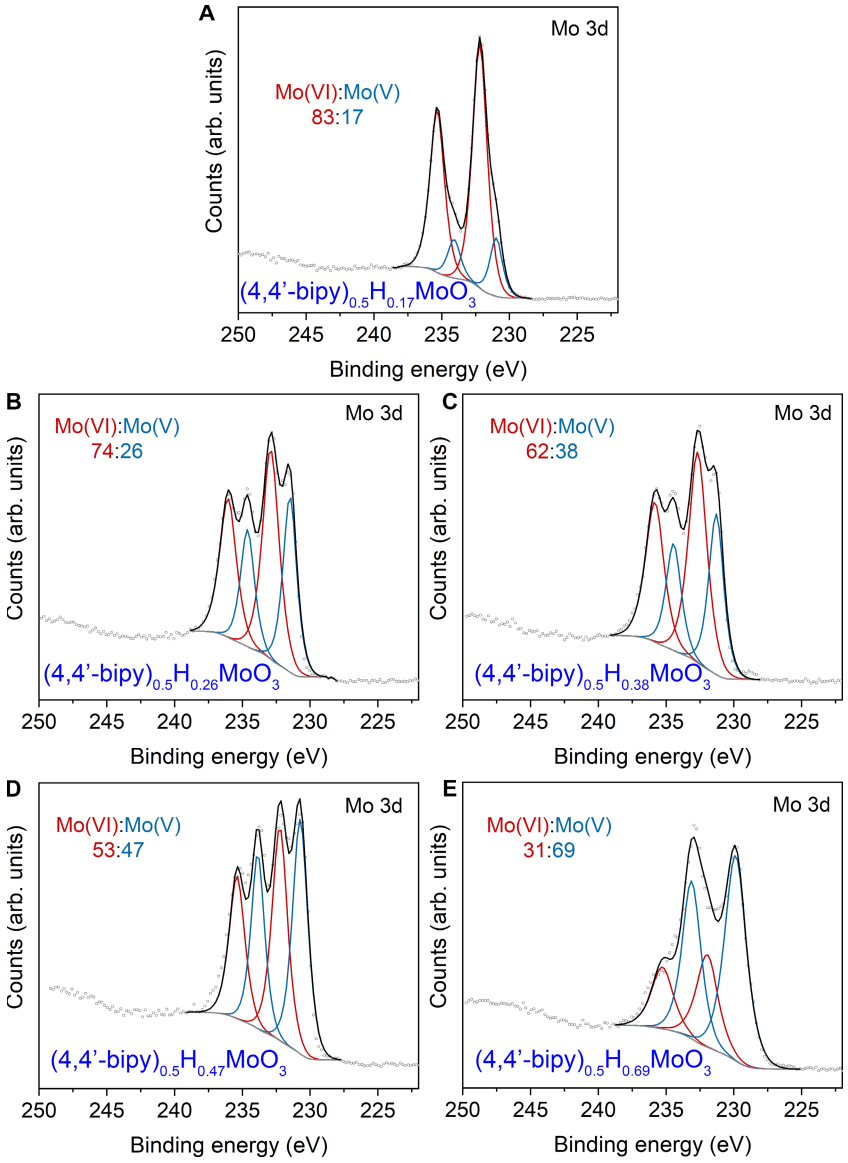

Figure S14. Mo 3d XPS spectra for $(4,4'\text{-bipy})_{0.5}H_xMoO_3$ with additional *x* values not shown in Fig. 4 of the main text. Individual peak fits are shown in red and blue. Peak fit backgrounds and envelopes are shown with gray and black lines, respectively. A) $(4,4'\text{-bipy})_{0.5}H_{0.17}MoO_3$. B) $(4,4'\text{-bipy})_{0.5}H_{0.26}MoO_3$. C) $(4,4'\text{-bipy})_{0.5}H_{0.38}MoO_3$. D) $(4,4'\text{-bipy})_{0.5}H_{0.47}MoO_3$. E) $(4,4'\text{-bipy})_{0.5}H_{0.69}MoO_3$.

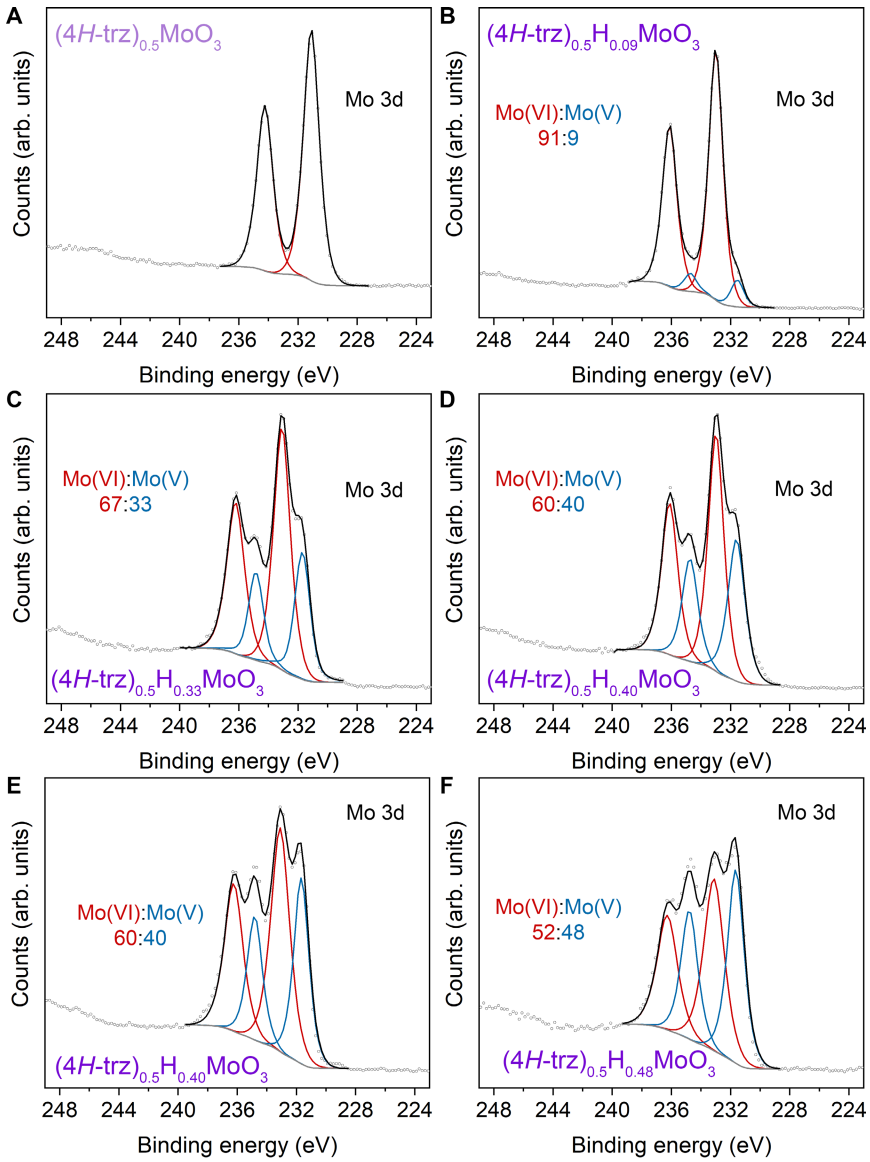

Figure S15. Mo 3d XPS spectra for $(4H\text{-trz})_{0.5}H_xMoO_3$. Individual peak fits are shown in red and blue. Peak fit backgrounds and envelopes are shown with gray and black lines, respectively. A) $(4H\text{-trz})_{0.5}MoO_3$. B) $(4H\text{-trz})_{0.5}H_{0.09}MoO_3$. C) $(4H\text{-trz})_{0.5}H_{0.33}MoO_3$. D) $(4H\text{-trz})_{0.5}H_{0.40}MoO_3$. E) $(4H\text{-trz})_{0.5}H_{0.40}MoO_3$. F) $(4H\text{-trz})_{0.5}H_{0.48}MoO_3$.

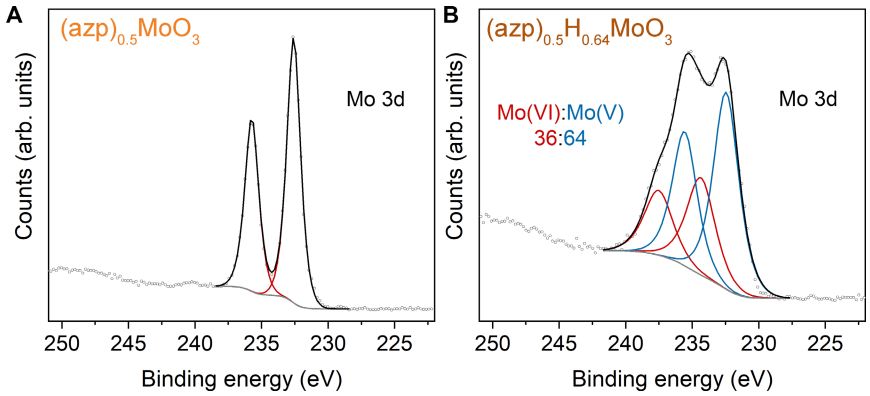

Figure S16. Mo 3d XPS spectra for $(azp)_{0.5}H_xMoO_3$. Individual peak fits are shown in red and blue. Peak fit backgrounds and envelopes are shown with gray and black lines, respectively. A) $(azp)_{0.5}MoO_3$. B) $(azp)_{0.5}H_{0.64}MoO_3$.

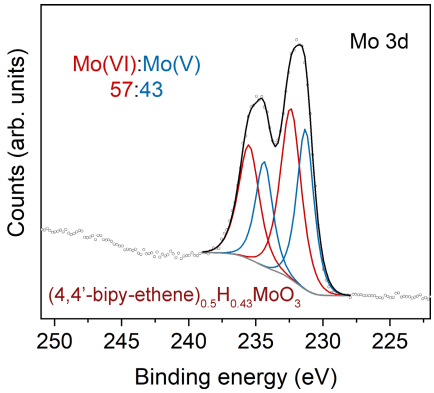

Figure S17. Mo 3d XPS spectra for $(4,4'\text{-bipy-ethene})_{0.5}H_{0.43}MoO_3$. Individual peak fits are shown in red and blue. Peak fit backgrounds and envelopes are shown with gray and black lines, respectively.

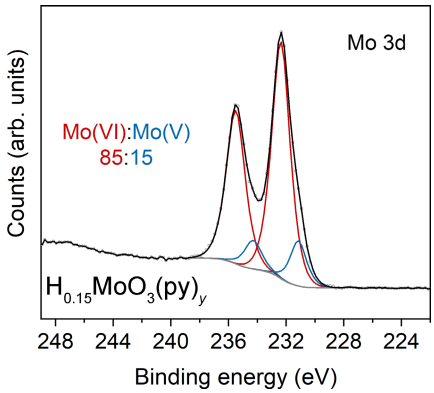

Figure S18. Mo 3d XPS spectra for $H_{0.15}MoO_3(py)_y$ (intercalated producted). Individual peak fits are shown in red and blue. Peak fit backgrounds and envelopes are shown with gray and black lines, respectively.

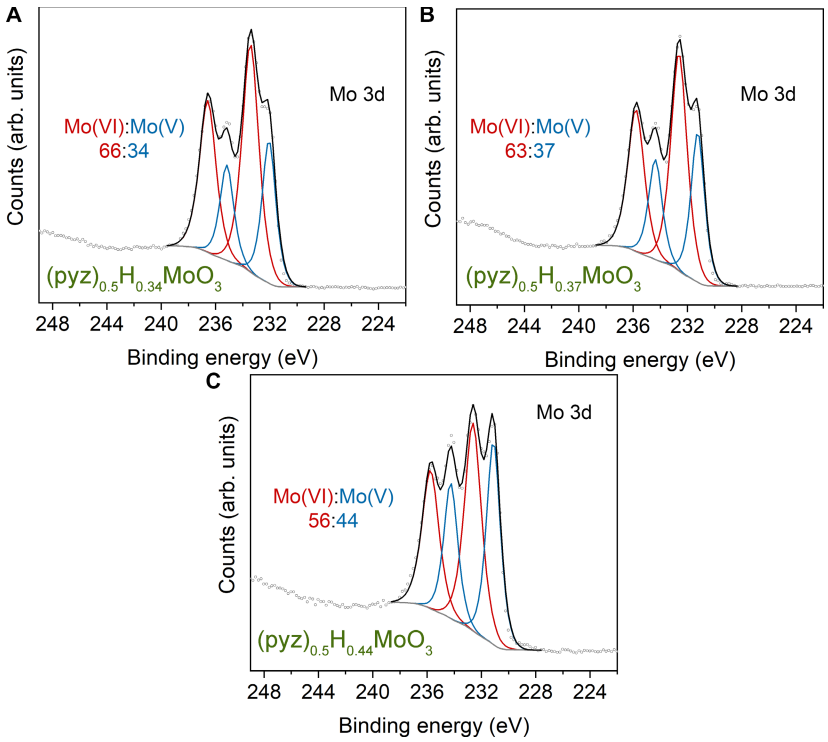

Figure S19. Mo 3d XPS spectra for $(pyz)_{0.5}H_xMoO_3$. Individual peak fits are shown in red and blue. Peak fit backgrounds and envelopes are shown with gray and black lines, respectively. A) $(pyz)_{0.5}H_{0.34}MoO_3$. B) $(pyz)_{0.5}H_{0.37}MoO_3$. C) $(pyz)_{0.5}H_{0.44}MoO_3$.

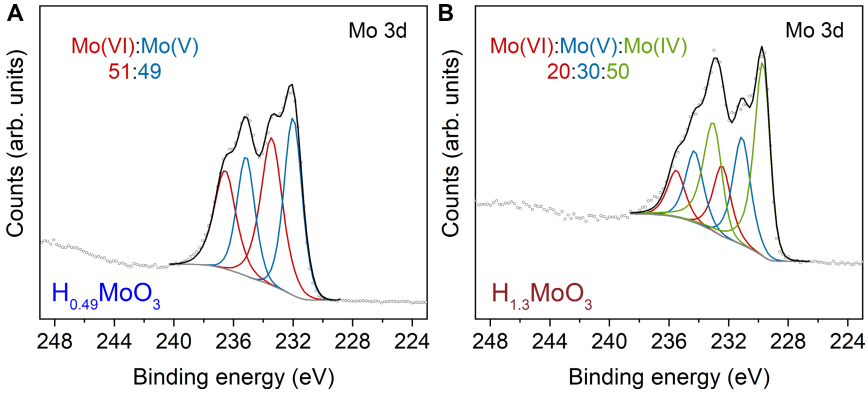

Figure S20. Mo 3d XPS spectra for H_xMoO_3 inorganic bronzes. Individual peak fits are shown in red, blue, and green. Peak fit backgrounds and envelopes are shown with gray and black lines, respectively. A) $H_{0.49}MoO_3$ (type I). B) $H_{1.3}MoO_3$ (type III). Given that $H_{0.95}MoO_3$ is synthesized by thermal conversion of type III, it is likely that type III is somewhat re-oxidized in the high-vacuum of the XPS chamber, leading to a slightly lower than expected value of *x*.

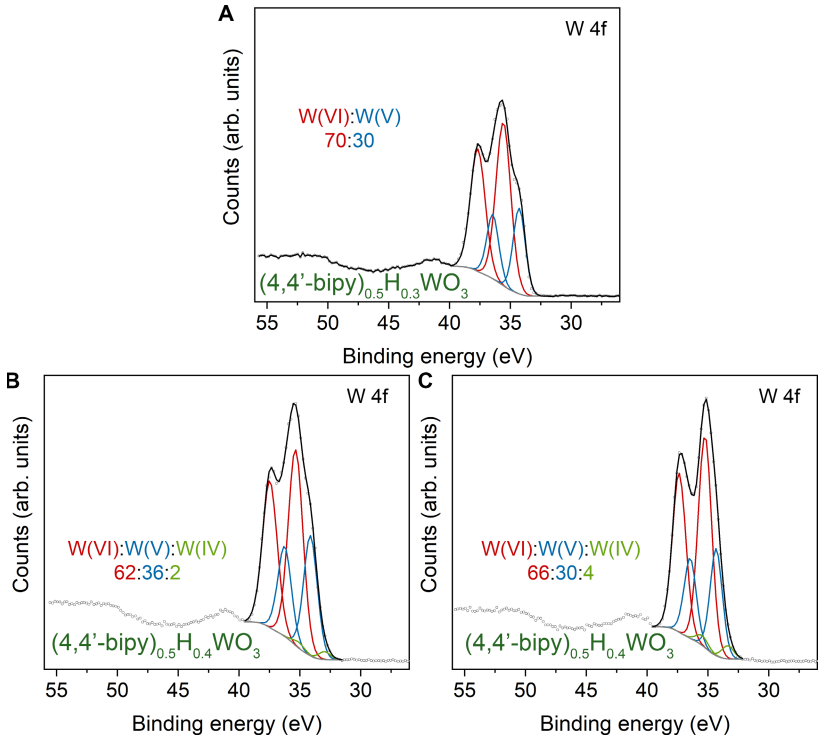

Figure S21. W 4f XPS spectra for (4,4'-bipy)$_{0.5}$H$_x$WO$_3$ with additional *x* values not shown in Fig. 4 of the main text. Individual peak fits are shown in red, blue, and green. Peak fit backgrounds and envelopes are shown with gray and black lines, respectively. A) (4,4'-bipy)$_{0.5}$H$_{0.3}$WO$_3$. B) (4,4'-bipy)$_{0.5}$H$_{0.4}$WO$_3$. C) (4,4'-bipy)$_{0.5}$H$_{0.4}$WO$_3$.

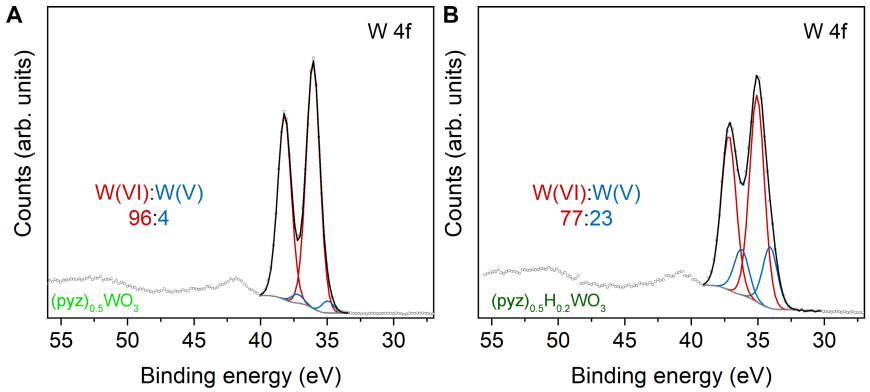

Figure S22. W 4f XPS spectra for (pyz)$_{0.5}$H$_x$WO$_3$. Individual peak fits are shown in red and blue. Peak fit backgrounds and envelopes are shown with gray and black lines, respectively. A) (pyz)$_{0.5}$WO$_3$. Note that the combination of high vacuum and charge neutralization in the XPS chamber are known to reduce W *in situ*, hence the small quantity of W(V) in the oxidized sample. B) (pyz)$_{0.5}$H$_{0.2}$WO$_3$.

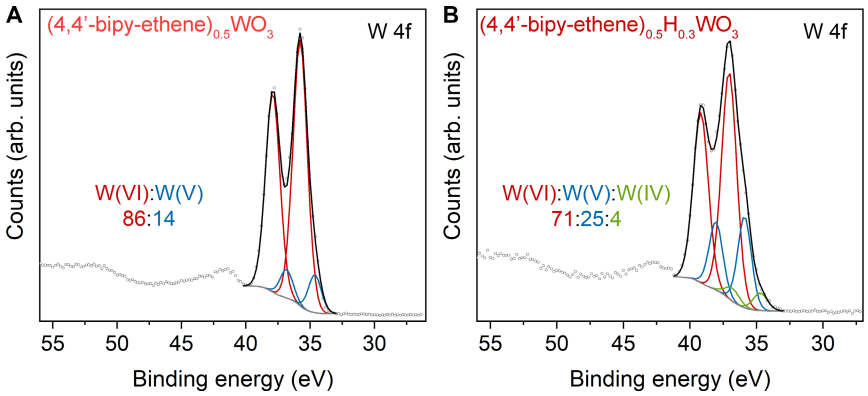

Figure S23. W 4f XPS spectra for (4,4'-bipy-ethene)$_{0.5}$H$_x$WO$_3$. Individual peak fits are shown in red, blue, and green. Peak fit backgrounds and envelopes are shown with gray and black lines, respectively. A) (4,4'-bipy-ethene)$_{0.5}$WO$_3$. Note that the combination of high vacuum and charge neutralization in the XPS chamber are known to reduce W *in situ*, hence the small quantity of W(V) in the oxidized sample. B) (4,4'-bipy-ethene)$_{0.5}$H$_{0.3}$WO$_3$.

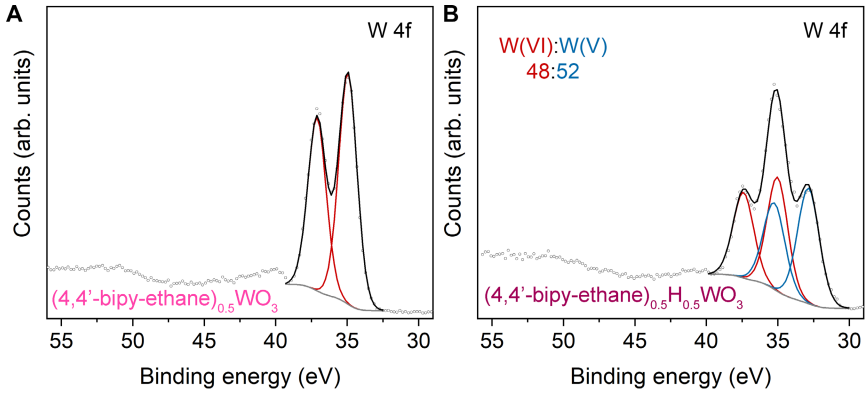

Figure S24. W 4f XPS spectra for (4,4'-bipy-ethane)$_{0.5}$H$_x$WO$_3$. Individual peak fits are shown in red and blue. Peak fit backgrounds and envelopes are shown with gray and black lines, respectively. A) (4,4'-bipy-ethane)$_{0.5}$WO$_3$. B) (4,4'-bipy-ethane)$_{0.5}$H$_{0.5}$WO$_3$.

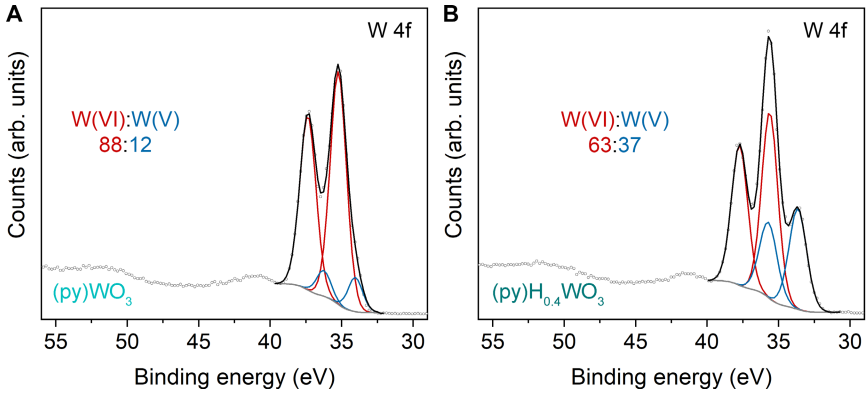

Figure S25. W 4f XPS spectra for (py)H$_x$WO$_3$. Individual peak fits are shown in red and blue. Peak fit backgrounds and envelopes are shown with gray and black lines, respectively. A) (py)WO$_3$. Note that the combination of high vacuum and charge neutralization in the XPS chamber are known to reduce W *in situ*, hence the small quantity of W(V) in the oxidized sample. B) (py)H$_{0.4}$WO$_3$.

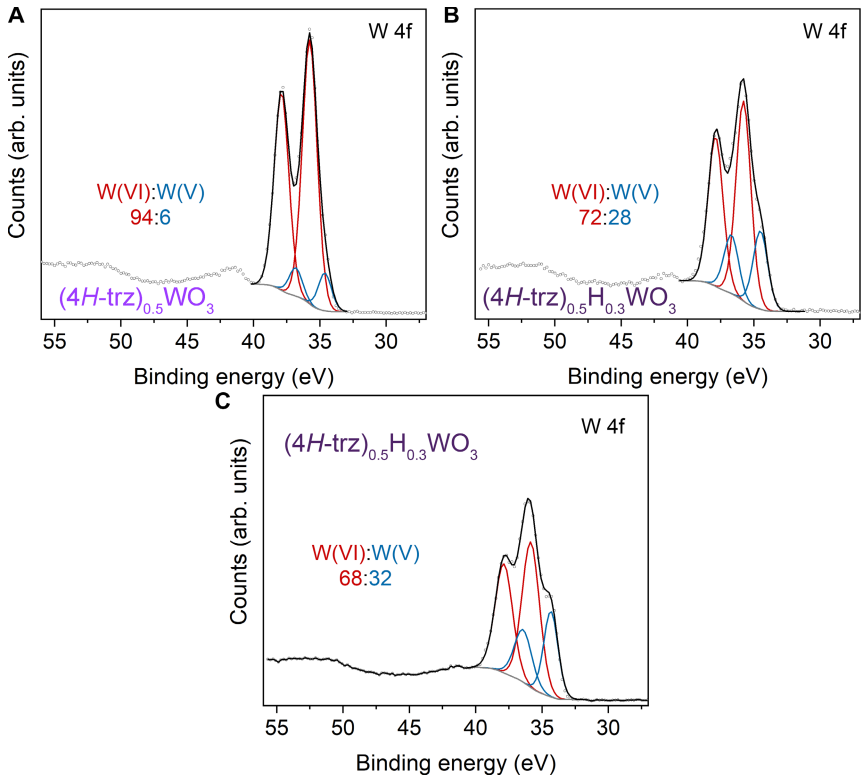

Figure S26. W 4f XPS spectra for $(4H\text{-trz})_{0.5}H_xWO_3$. Individual peak fits are shown in red, blue, and green. Peak fit backgrounds and envelopes are shown with gray and black lines, respectively. A) $(4H\text{-trz})_{0.5}WO_3$. Note that the combination of high vacuum and charge neutralization in the XPS chamber are known to reduce W *in situ*, hence the small quantity of W(V) in the oxidized sample. B) $(4H\text{-trz})_{0.5}H_{0.3}WO_3$. C) $(4H\text{-trz})_{0.5}H_{0.3}WO_3$.

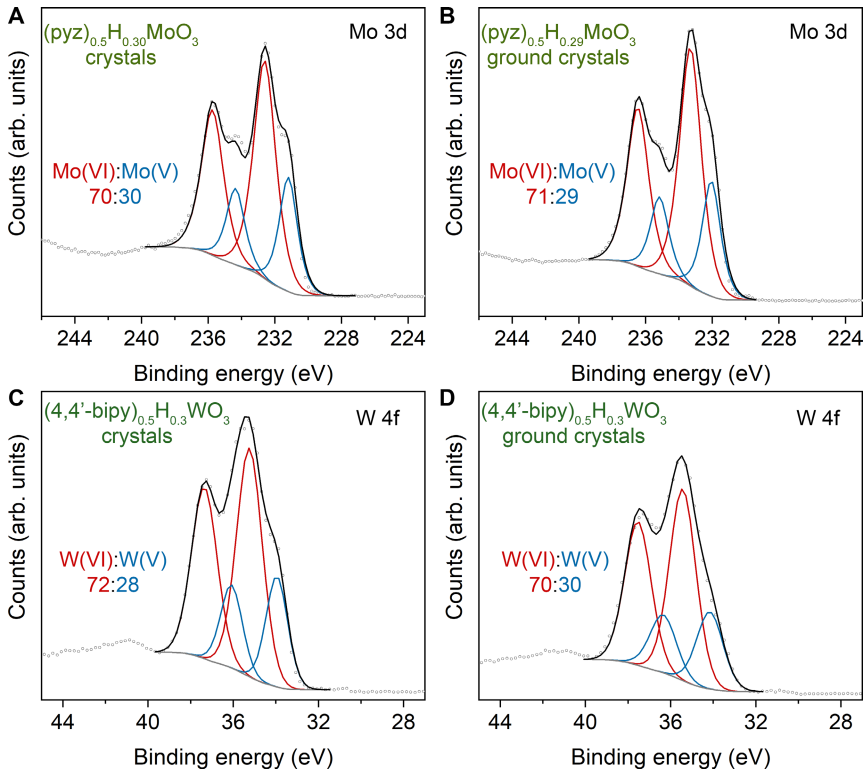

Figure S27. Mo 3d XPS spectra for **A**) crystals and **B**) ground crystals of $(pyz)_{0.5}H_xMoO_3$. W 4f XPS spectra for **C**) crystals and **D**) ground crystals of $(4,4'\text{-bipy})_{0.5}H_xWO_3$. Individual peak fits are shown in red and blue. Peak fit backgrounds and envelopes are shown with gray and black lines, respectively.

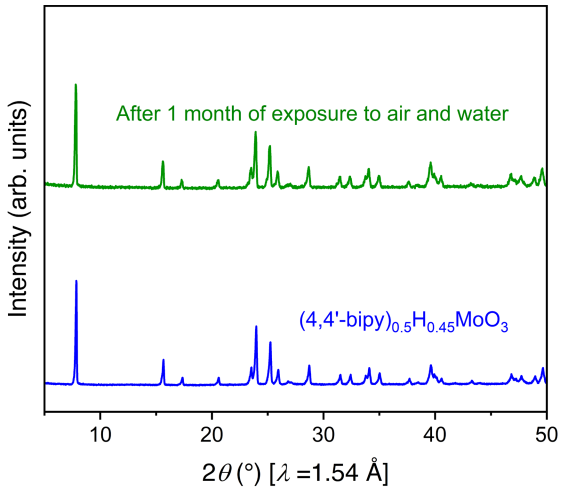

Figure S28. Powder X-ray diffraction (PXRD) patterns for $(4,4'\text{-bipy})_{0.5}H_{0.45}MoO_3$ **A**) before and **B**) after submersion in water in air for one month.

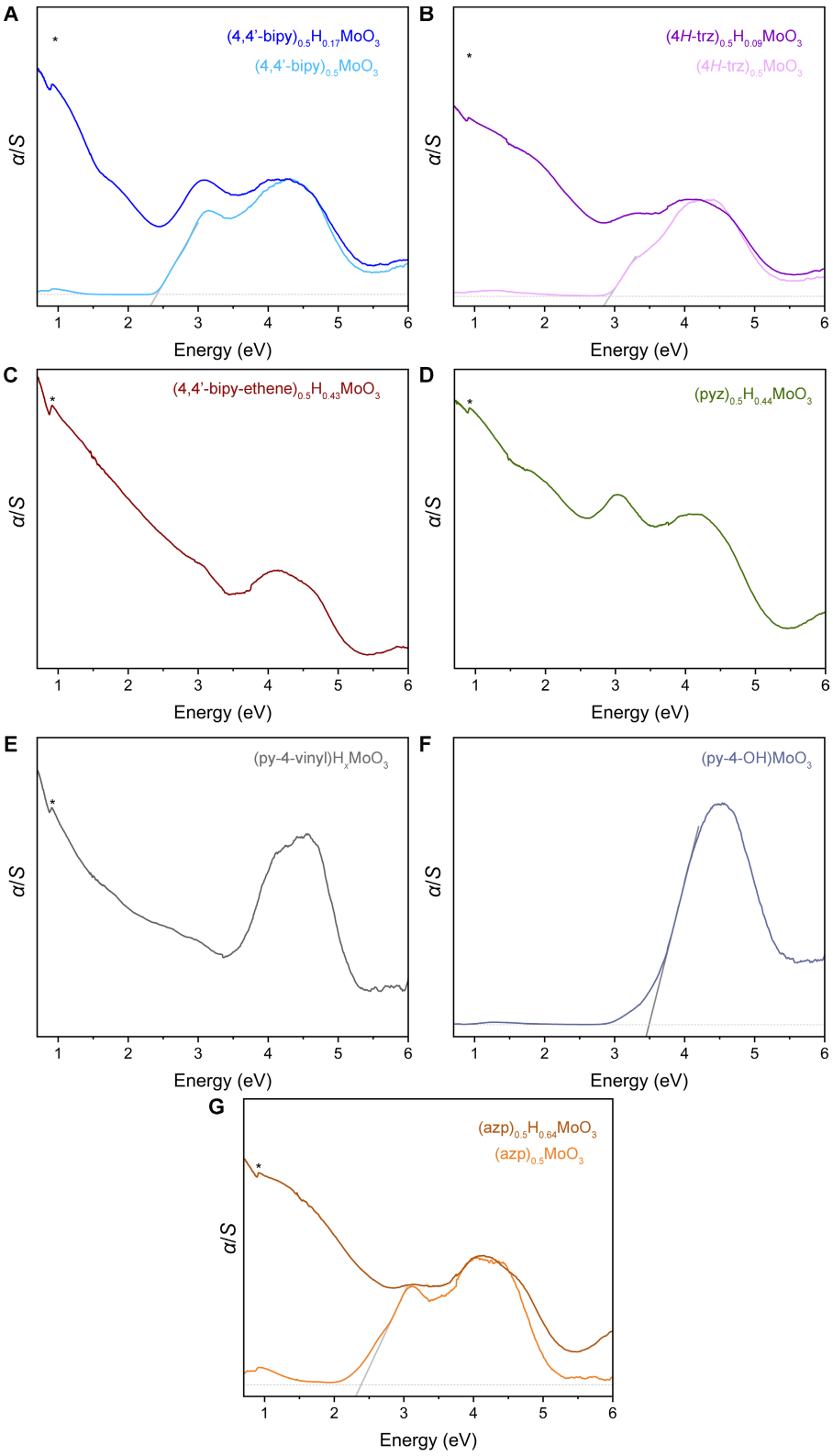

Figure S29. Diffuse reflectance spectra for hybrid molybdenum bronzes and their oxidized analogs. Linear extrapolations to determine bandgap are shown with gray lines for the oxidized analogs. $BaSO_4$ background peaks are indicated with an asterisk. **A**) $(4,4'\text{-bipy})_{0.5}H_xMoO_3$ (x = 0, 0.17). **B**) $(4H\text{-trz})_{0.5}H_xMoO_3$ (x = 0, 0.09). **C**) $(4,4'\text{-bipy-ethene})_{0.5}H_{0.43}MoO_3$. **D**) $(pyz)_{0.5}H_{0.44}MoO_3$. **E**) $(py\text{-}4\text{-vinyl})H_xMoO_3$. **F**) $(py\text{-}4\text{-OH})MoO_3$. **G**) $(azp)_{0.5}H_xMoO_3$ (x = 0, 0.64). Note that the extrapolation for azp was carried out from a higher-energy region of the spectrum since azp itself absorbs ca. 2.5 eV (Fig. S31).

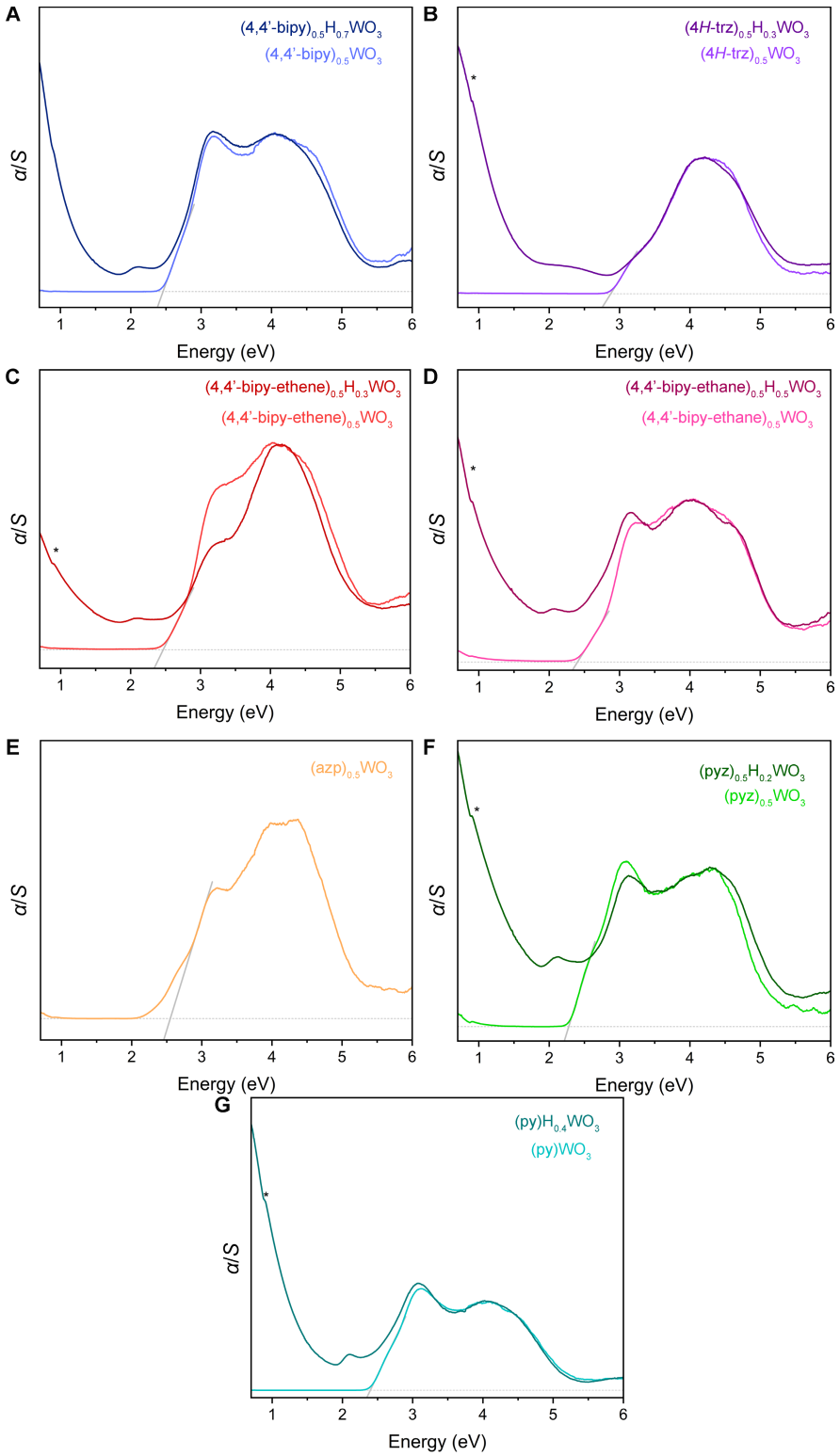

Figure S30. Diffuse reflectance spectra for hybrid tungsten bronzes and their oxidized analogs. Linear extrapolations to determine bandgap are shown with gray lines for the oxidized analogs. $BaSO_4$ background peaks are indicated with an asterisk. **A**) (4,4'-bipy)$_{0.5}$H$_x$WO$_3$ (x = 0, 0.7). **B**) (4*H*-trz)$_{0.5}$H$_x$WO$_3$ (x = 0, 0.3). **C**) (4,4'-bipy-ethene)$_{0.5}$H$_x$WO$_3$ (x = 0, 0.3). **D**) (4,4'-bipy-ethane)$_{0.5}$H$_x$WO$_3$ (x = 0, 0.5). **E**) (azp)$_{0.5}$WO$_3$. Note that the extrapolation for azp was carried out from a higher-energy region of the spectrum since azp itself absorbs ca. 2.5 eV (Fig. S31). **F**) (pyz)$_{0.5}$H$_x$WO$_3$ (x = 0, 0.2). **G**) (py)H$_x$WO$_3$ (x = 0, 0.4).

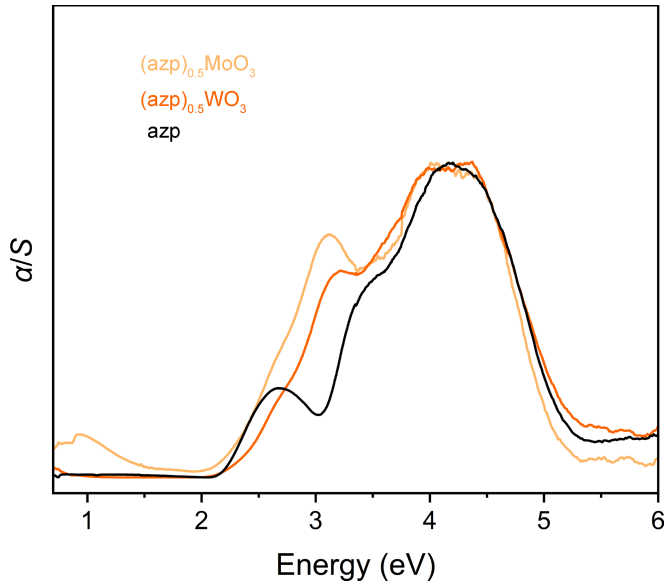

Figure S31. Diffuse reflectance spectra for $(azp)_{0.5}WO_3$, $(azp)_{0.5}MoO_3$, and azp showing absorption ca. 2.5 eV for the ligand alone, necessitating extrapolation from higher energy portions of the hybrid metal oxide spectra in order to determine band gap.

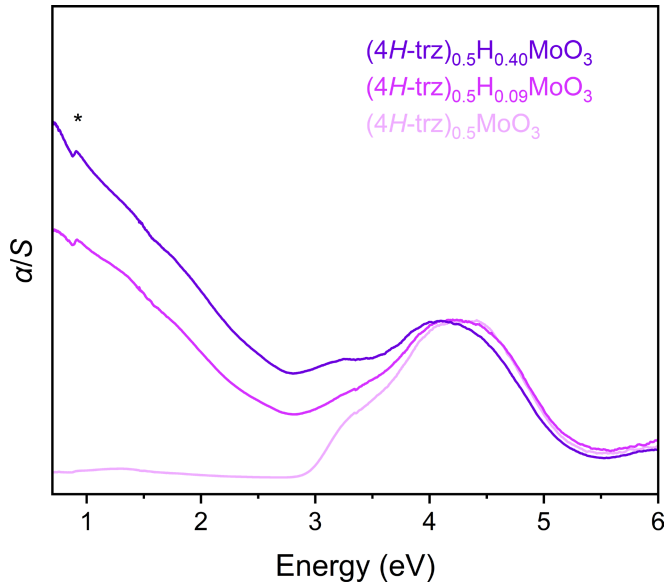

Figure S32. Diffuse reflectance spectra for $(4H\text{-trz})_{0.5}H_xMoO_3$ (x = 0, 0.09, 0.40). $BaSO_4$ background peaks are indicated with an asterisk.

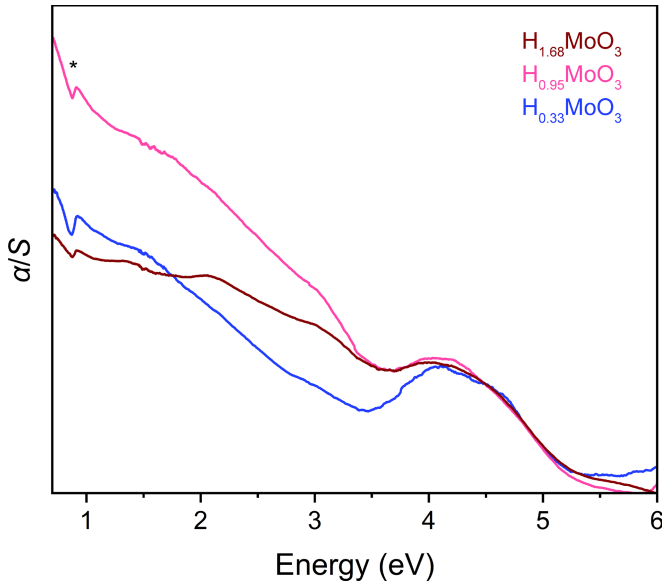

Figure S33. Diffuse reflectance spectra for H_xMoO_3 where $x = 0.33, 0.95, 1.68$. Here, these values of x are nominal values assigned according to agreement of these samples' powder X-ray diffraction patterns to reported structures (see Fig. S2). $BaSO_4$ background peaks are indicated with an asterisk.

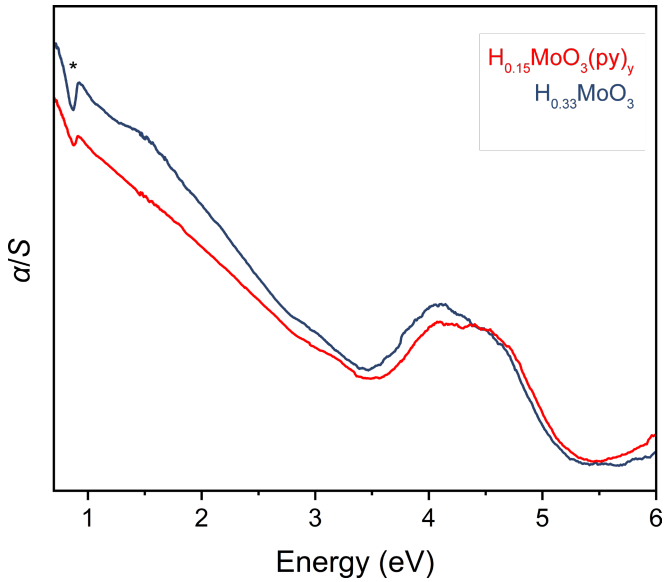

Figure S34. Diffuse reflectance spectra for the intercalation compound $H_{0.15}MoO_3(py)_y$ compared with $H_{0.33}MoO_3$. $BaSO_4$ background peaks are indicated with an asterisk.

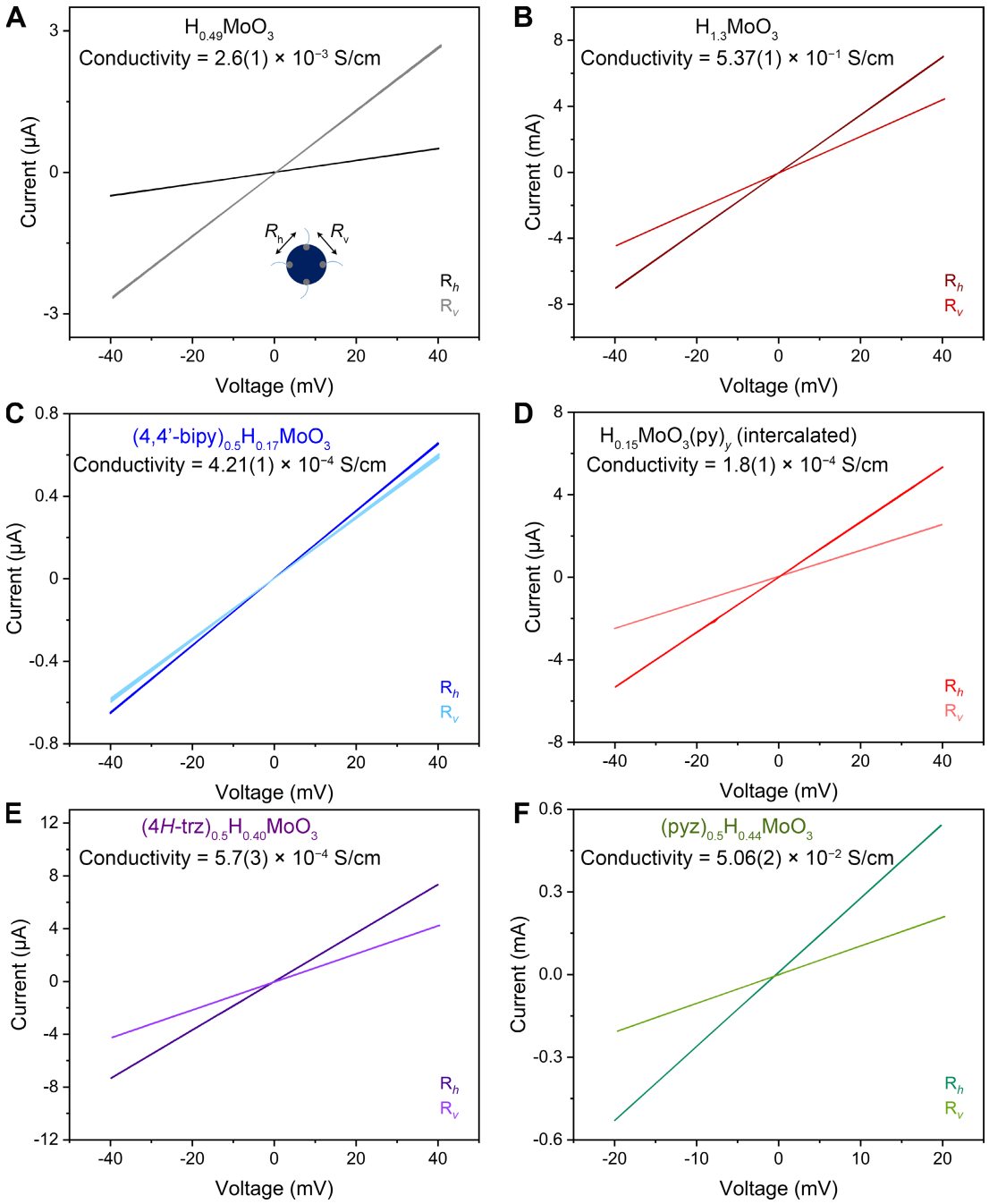

Figure S35. Room temperature four-point *I–V* measurements on pressed powder pellets of hybrid molybdenum bronzes. Sheet resistances and subsequent conductivities were calculated using all four possible combinations of R_h and R_v according to the van der Pauw method described above, however, for the sake of clarity only one representative set is shown for each material. **A**) $H_{0.49}MoO_3$. **B**) $H_{1.3}MoO_3$. **C**) $(4,4'\text{-bipy})_{0.5}H_{0.17}MoO_3$. **D**) $H_{0.15}MoO_3(py)_y$. **E**) $(4H\text{-trz})_{0.5}H_{0.40}MoO_3$. **F**) $(pyz)_{0.5}H_{0.44}MoO_3$.

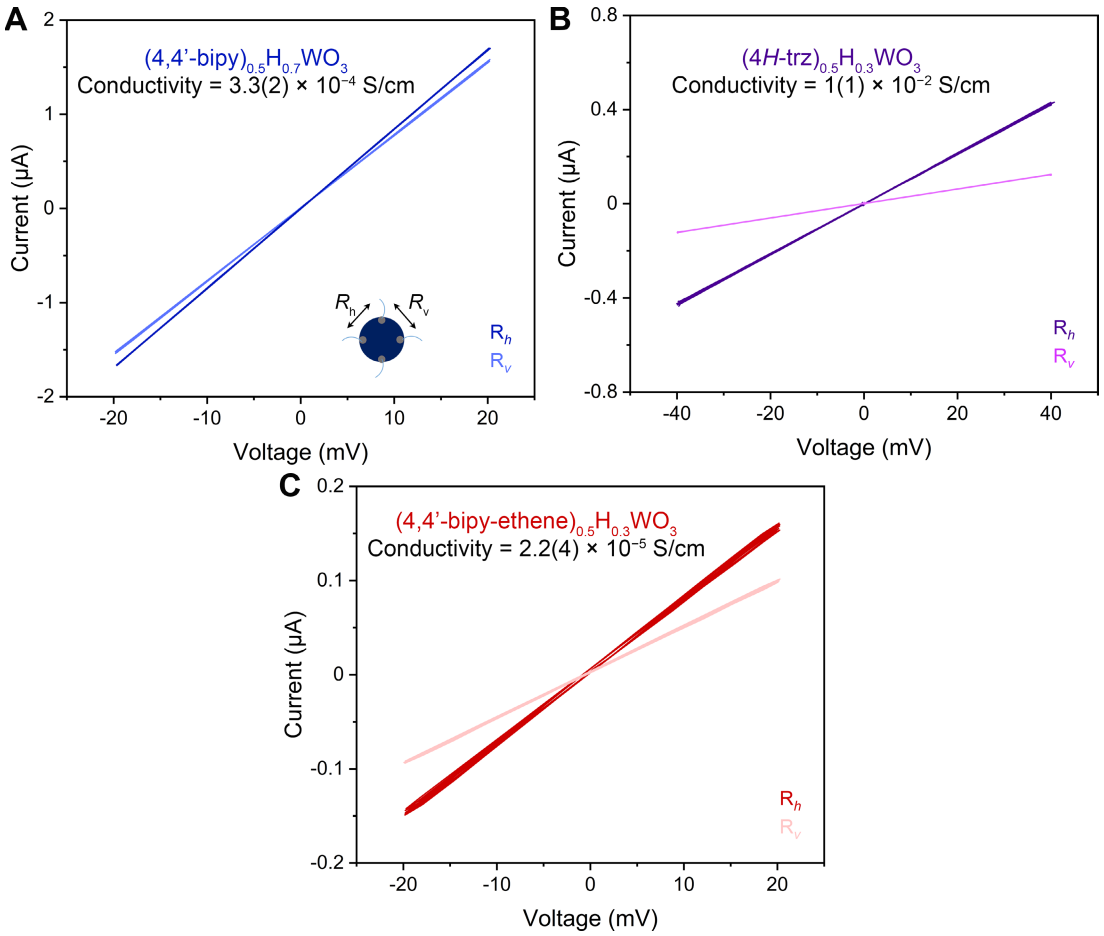

Figure S36. Room temperature four-point *I–V* measurements on pressed powder pellets of hybrid tungsten bronzes. Sheet resistances and subsequent conductivities were calculated using all four possible combinations of R_h and R_v according to the van der Pauw method described above, however, for the sake of clarity only one representative set is shown for each material. **A**) (4,4'-bipy)$_{0.5}$H$_{0.7}$WO$_3$. **B**) (4*H*-trz)$_{0.5}$H$_{0.3}$WO$_3$. **C**) (4,4'-bipy-ethene)$_{0.5}$H$_{0.3}$WO$_3$.

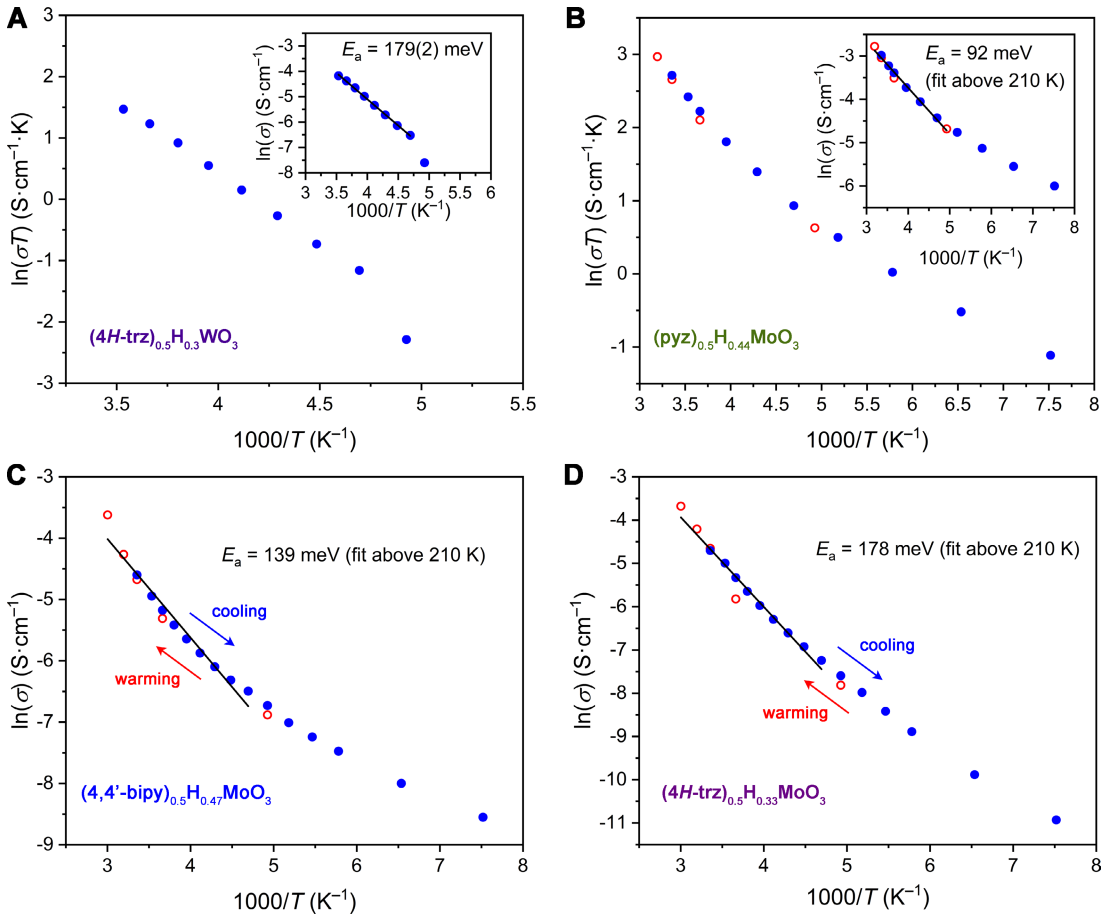

Figure S37. Variable-temperature four-point conductivity measurements on pressed powder pellets of hybrid bronzes, plotted as $\ln(\sigma T)$ vs. 1000/T according to the polaronic model of charge transport and/or $\ln(\sigma)$ vs. 1000/T according to the Arrhenius model of charge transport. Activation energies of conduction, E_a, are determined from linear fits in the Arrhenius plots. **A**) $(4H\text{-trz})_{0.5}H_{0.3}WO_3$ (polaronic and Arrhenius inset). **B**) $(pyz)_{0.5}H_{0.44}MoO_3$ (polaronic and Arrhenius inset). **C**) $(4,4'\text{-bipy})_{0.5}H_{0.47}MoO_3$ (Arrhenius). **D**) $(4H\text{-trz})_{0.5}H_{0.33}MoO_3$ (Arrhenius).

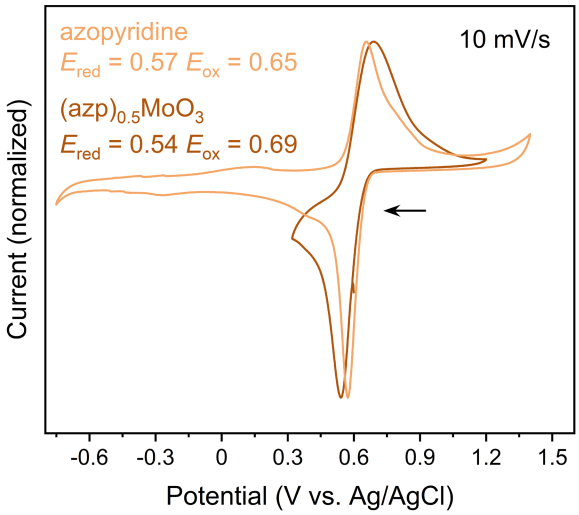

Figure S38. Cyclic voltammogram for $(azp)_{0.5}MoO_3$ compared to azp alone in 1 M H_2SO_4. The arrow indicates the direction of the initial scan.

References

(1) Birtill, J. J.; Dickens, P. G. Phase relationships in the system H_xMoO_3 ($0<x\leqslant 2.0$). *Mater. Res. Bull.* **1978**, *13*, 311–316.

(2) Schöllhorn, R.; Schulte-Nölle, T.; Steinhoff, G. Layered intercalation complexes of the hydrogen bronze $H_{0.5}MoO_3$ with organic lewis bases. *J. Less-Common Met.* **1980**, *71*, 71–78.

(3) Zhang, X.; Hejazi, M.; Thiagarajan, S. J.; Woerner, W. R.; Banerjee, D.; Emge, T. J.; Xu, W.; Teat, S. J.; Gong, Q.; Safari, A.; Yang, R.; Parise, J. B.; Li, J. From 1D Chain to 3D Network: A New Family of Inorganic–Organic Hybrid Semiconductors $MO_3(L)_x$ (M = Mo, W; L = Organic Linker) Built on Perovskite-like Structure Modules. *J. Am. Chem. Soc.* **2013**, *135*, 17401–17407.

(4) Hagrman, P. J.; LaDuca, R. L.; Koo, H. J.; Rarig, R.; Haushalter, R. C.; Whangbo, M.-H.; Zubieta, J. Ligand Influences on the Structures of Molybdenum Oxide Networks. *Inorg. Chem.* **2000**, *39*, 4311–4317.

(5) Yan, B.; Xu, Y.; Goh, N. K.; Chia, L. S. Hydrothermal synthesis and crystal structures of two novel hybrid open-frameworks and a two-dimensional network based on tungsten(VI) oxides. *Chem. Commun.* **2000**, 2169–2170.

(6) Amarante, T. R.; Neves, P.; Valente, A. A.; Paz, F. A. A.; Pillinger, M.; Gonçalves, I. S. Metal oxide-triazole hybrids as heterogeneous or reaction-induced self-separating catalysts. *J. Catal.* **2016**, *340*, 354–367.

(7) Johnson, J. W.; Jacobson, A. J.; Rich, S. M.; Brody, J. F. New layered compounds with transition-metal oxide layers separated by covalently bound organic ligands. Molybdenum and tungsten trioxide-pyridine. *J. Am. Chem. Soc.* **1981**, *103*, 5246–5247.

(8) Bruker AXS Inc.: Madison, Wisconsin, 2021.

(9) Bruker AXS Inc.: Madison, Wisconsin, 2016.

(10) Sheldrick, G. M. Göttingen, 1997.

(11) Sheldrick, G. SHELXT - Integrated space-group and crystal-structure determination. *Acta Crystallogr. Sect. A: Found. Crystallogr.* **2015**, *A71*, 3–8.

(12) Sheldrick, G. M. A short history of SHELX. *Acta Crystallogr. Sect. A: Found. Crystallogr.* **2008**, *A64*, 112–122.

(13) Sheldrick, G. Crystal structure refinement with SHELXL. *Acta Cryst. Sect. B* **2015**, *C71*, 3–8.

(14) Dolomanov, O. V.; Bourhis, L. J.; Gildea, R. J.; Howard, J. A. K.; Puschmann, H. OLEX2: a complete structure solution, refinement and analysis program. *J. Appl. Crystallogr.* **2009**, *42*, 339–341.

(15) Müller, P., Herbst-Irmer, R., Spek, A. L., Schneider, T. R., Sawaya, M. R. *Crystal Structure Refinement: A Crystallographer's Guide to SHELXL*; Muller, P., Ed.; Oxford University Press: New York, 2006.

(16) Toby, B. H.; Von Dreele, R. B. GSAS-II: the genesis of a modern open-source all purpose crystallography software package. *J. Appl. Crystallogr.* **2013**, *46*, 544–549.

(17) Major, G. H.; Fairley, N.; Sherwood, P. M. A.; Linford, M. R.; Terry, J.; Fernandez, V.; Artyushkova, K. Practical guide for curve fitting in X-ray photoelectron spectroscopy. *J. Vac. Sci. Technol., A* **2020**, *38*, 061203.

(18) Suzuki, N.; Yabuki, K.; Oshimura, N.; Yoshio, S.; Adachi, K. X-ray Photoelectron Spectroscopic Study of Reduced Alkali Tungsten Oxides with Localized and Delocalized Electrons. *J. Phys. Chem. C* **2022**, *126*, 15436–15445.

(19) Shubert-Zuleta, S. A.; Tandon, B.; Roman, B. J.; Gan, X. Y.; Milliron, D. J. How to Quantify Electrons in Plasmonic Colloidal Metal Oxide Nanocrystals. *Chem. Mater.* **2023**, *35*, 3880–3891.

(20) Kubelka, P.; Munk, F. Z. Ein Beitrag Zur Optik Der Farbanstriche. *Z. Tech. Phys.* **1931**, *12*, 593–601.

(21) Tauc, J. Optical properties and electronic structure of amorphous Ge and Si. *Mater. Res. Bull.* **1968**, *3*, 37–46.

(22) Brown, I. D. *The Chemical Bond in Inorganic Chemistry: The Bond Valence Model*; Oxford University Press, 2006.
(23) Brown, I. D. Recent Developments in the Methods and Applications of the Bond Valence Model. *Chem. Rev.* **2009**, *109*, 6858–6919.
(24) Zocchi, F. Critical comparison of equations correlating valence and length of a chemical bond. Evaluation of the parameters R_1 and B for the M–O bond in MoO_6 octahedra. *Solid State Sci.* **2000**, *2*, 385–389.
(25) Ma, Z.; Shi, X.-M.; Nishimura, S.-i.; Ko, S.; Okubo, M.; Yamada, A. Anhydrous Fast Proton Transport Boosted by Hydrogen Bond Network in A Dense Oxide-ion Array of α-MoO_3. *Adv. Mater.* **2022**, *34*, 2203335.
(26) Glemser, O.; Lutz, G. Über Molybdänblau. *Z. Anorg. Allg. Chem.* **1951**, *264*, 17–33.